学位論文

Inflammation-driven senescence-associated secretory phenotype in cancer-associated fibroblasts enhances peritoneal dissemination
（炎症下で誘導される癌性腹水中の老化 CAFs は腹膜播種を促進する）

安田　忠仁

Tadahito　Yasuda

指導教員

馬場　秀夫　教授

熊本大学大学院医学教育部博士課程医学専攻消化器外科学

2021 年度

学　位　論　文

論文題名　：　**Inflammation-driven senescence-associated secretory phenotype in cancer-associated fibroblasts enhances peritoneal dissemination**

(炎症下で誘導される癌性腹水中の老化 CAFs は腹膜播種を促進する)

著 者 名　：　安田　忠仁

Tadahito　Yasuda

指導教員名　：　熊本大学大学院医学教育部博士課程医学専攻消化器外科学　馬場　秀夫　教授

審査委員名　：　分子生理学担当教授　富澤　一仁

発生制御部門　細胞医学分野担当教授　中尾　光善

呼吸器外科学担当教授　鈴木　実

2021年度

Cell Reports

Article

Inflammation-driven senescence-associated secretory phenotype in cancer-associated fibroblasts enhances peritoneal dissemination

Graphical Abstract

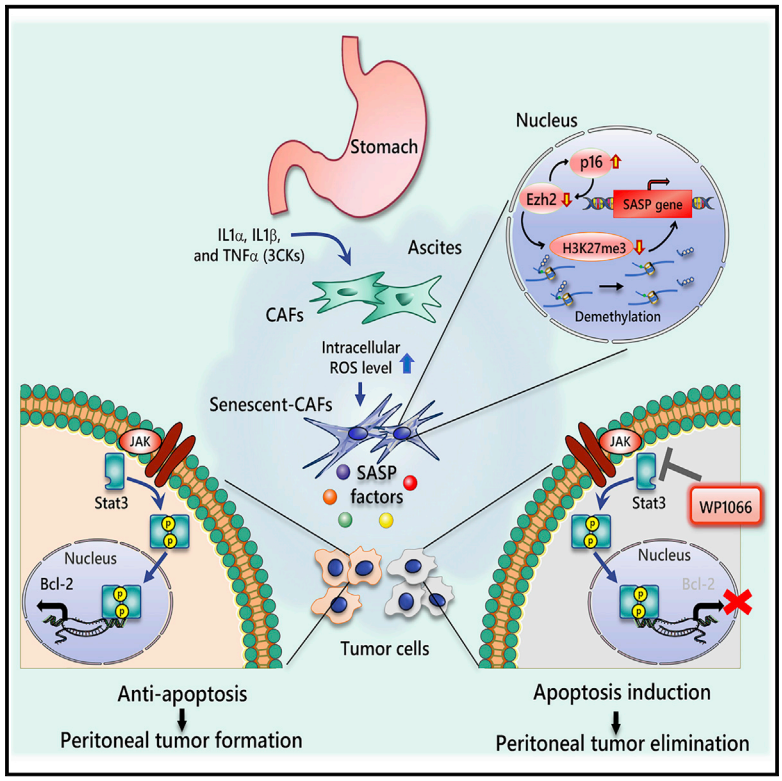

Highlights

- EZH2 downregulation leads to SASP maintenance through depletion of H3K27me3 marks
- Senescent CAFs in ascites of GC patients with peritoneal dissemination exhibit SASP
- Senescent CAFs enhance the peritoneal tumor formation through JAK/STAT3 signaling
- A JAK inhibitor blocks peritoneal tumor formation driven by systemic inflammation

Authors

Tadahito Yasuda, Mayu Koiwa, Atsuko Yonemura, ..., Patrick Tan, Hideo Baba, Takatsugu Ishimoto

Correspondence

hdobaba@kumamoto-u.ac.jp (H.B.), taka1516@kumamoto-u.ac.jp (T.I.)

In brief

Yasuda et al. show the fundamental mechanism by which inflammation-driven senescent CAFs enhance the peritoneal dissemination and the significance of targeting senescent CAFs as well as JAK/STAT3 signaling in GC cells. These findings provide a promising therapeutic approach for GC peritoneal dissemination driven by systemic inflammation.

Yasuda et al., 2021, Cell Reports *34*, 108779
February 23, 2021
https://doi.org/10.1016/j.celrep.2021.108779

CellPress

Cell Reports

CellPress
OPEN ACCESS

Article

Inflammation-driven senescence-associated secretory phenotype in cancer-associated fibroblasts enhances peritoneal dissemination

Tadahito Yasuda,[1,2,10] Mayu Koiwa,[1,2,10] Atsuko Yonemura,[1,2] Keisuke Miyake,[1,2] Ryusho Kariya,[5] Sho Kubota,[7] Takako Yokomizo-Nakano,[7] Noriko Yasuda-Yoshihara,[1] Tomoyuki Uchihara,[1,2] Rumi Itoyama,[1,2] Luke Bu,[1,2] Lingfeng Fu,[1,2] Kota Arima,[1,2] Daisuke Izumi,[1] Shiro Iwagami,[1] Kojiro Eto,[1] Masaaki Iwatsuki,[1] Yoshifumi Baba,[1] Naoya Yoshida,[1] Hiroto Ohguchi,[4] Seiji Okada,[5] Keisuke Matsusaki,[6] Goro Sashida,[7] Akiko Takahashi,[8] Patrick Tan,[9] Hideo Baba,[1,3,*] and Takatsugu Ishimoto[1,2,11,*]

[1]Department of Gastroenterological Surgery, Graduate School of Medical Sciences, Kumamoto University, Kumamoto, Japan
[2]Gastrointestinal Cancer Biology, International Research Center for Medical Sciences (IRCMS), Kumamoto University, Kumamoto, Japan
[3]Center for Metabolic Regulation of Healthy Aging, Faculty of Life Sciences, Kumamoto University, Kumamoto, Japan
[4]Division of Disease Epigenetics, Institute of Resource Development and Analysis, Kumamoto University, Kumamoto, Japan
[5]Division of Hematopoiesis, Joint Research Center for Human Retrovirus Infection, Kumamoto University, Kumamoto, Japan
[6]Kanamecho Hospital, Tokyo, Japan
[7]Laboratory of Transcriptional Regulation in Leukemogenesis, International Research Center for Medical Sciences (IRCMS), Kumamoto University, Kumamoto, Japan
[8]The Cancer Institute, Japanese Foundation for Cancer Research, Tokyo, Japan
[9]Program in Cancer and Stem Cell Biology, Duke-NUS Medical School, Singapore, Singapore
[10]These authors contributed equally
[11]Lead contact
*Correspondence: hdobaba@kumamoto-u.ac.jp (H.B.), taka1516@kumamoto-u.ac.jp (T.I.)
https://doi.org/10.1016/j.celrep.2021.108779

SUMMARY

In the tumor microenvironment, senescent non-malignant cells, including cancer-associated fibroblasts (CAFs), exhibit a secretory profile under stress conditions; this senescence-associated secretory phenotype (SASP) leads to cancer progression and chemoresistance. However, the role of senescent CAFs in metastatic lesions and the molecular mechanism of inflammation-related SASP induction are not well understood. We show that pro-inflammatory cytokine-driven EZH2 downregulation maintains the SASP by demethylating H3K27me3 marks in CAFs and enhances peritoneal tumor formation of gastric cancer (GC) through JAK/STAT3 signaling in a mouse model. A JAK/STAT3 inhibitor blocks the increase in GC cell viability induced by senescent CAFs and peritoneal tumor formation. Single-cell mass cytometry revealed that fibroblasts exist in the ascites of GC patients with peritoneal dissemination, and the fibroblast population shows p16 expression and SASP factors at high levels. These findings provide insights into the inflammation-related SASP maintenance by histone modification and the role of senescent CAFs in GC peritoneal dissemination.

CONTEXT AND SIGNIFICANCE

Development of novel therapeutic strategy is required to overcome the peritoneal dissemination in advanced GC patients. However, conventional therapies do not demonstrate satisfying benefits in GC patients with peritoneal dissemination. This obstacle may be caused by non-malignant cells, not cancer cells themselves. Our findings reveal the fundamental mechanism by which inflammation-driven senescent CAFs enhance peritoneal dissemination. We also identified the significance of targeting senescent CAFs, as well as JAK/STAT3 signaling in GC cells. This study demonstrates a promising therapeutic approach for GC peritoneal dissemination driven by systemic inflammation.

INTRODUCTION

Gastric cancer (GC) is one of the most common cancers worldwide and is the third leading cause of cancer-related deaths in both men and women (Bray et al., 2018). Despite curative resection for advanced GCs, unresectable recurrence is often observed, and the prognosis of recurrent GC patients remains poor (Thomassen et al., 2014). The most frequent cause of GC death is peritoneal metastasis, which is considered an independent prognostic factor for poor prognosis (Chau et al., 2004). Peritoneal metastasis is caused by cancer cell dissemination into the peritoneal cavity from the primary organ. A poor understanding of the molecular mechanisms underlying the peritoneal dissemination process hinders the development of an effective

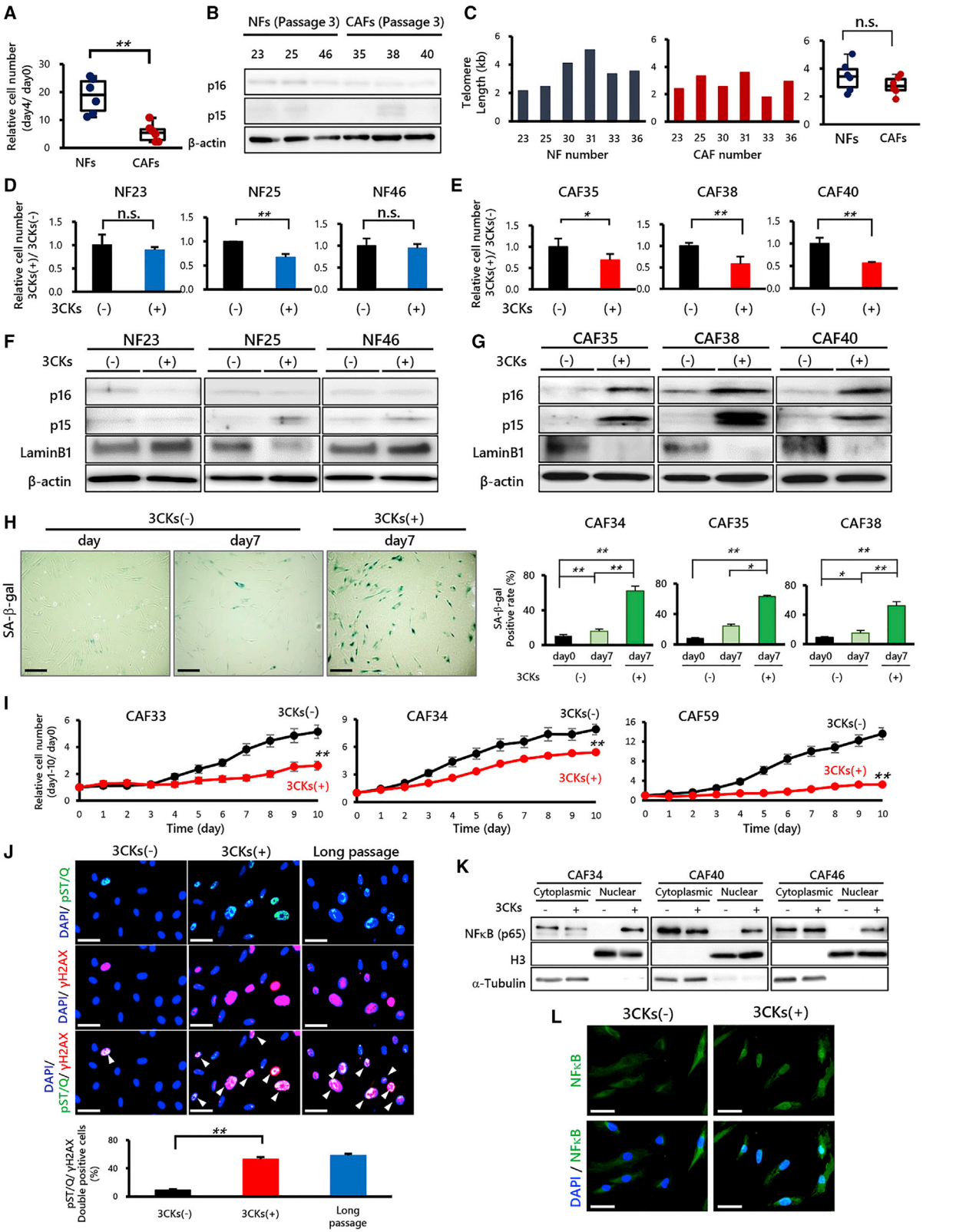

(legend on next page)

treatment strategy for this condition. In advanced GCs, cancer cells tend to interact with the tumor microenvironment, which contains extracellular matrix, immune cells, and cancer-associated fibroblasts (CAFs), and the interaction enhances cancer progression and metastasis through various cytokines and growth factors (Kalluri, 2016; Quail and Joyce, 2013). Although invasive cancer cells are likely to penetrate the gastric wall by interacting with the tumor microenvironment and spread into the peritoneal cavity, the role of non-malignant cells co-existing with cancer cells in mediating peritoneal dissemination is still unknown.

Chronic inflammation caused by *Helicobacter pylori* infection is the main risk factor for the development of GC. Therefore, various types of cells in the gastric mucosa are exposed to an inflammatory environment for long periods that induces epigenetic alterations (Ushijima and Hattori, 2012; Ishimoto et al., 2015). Moreover, several lines of evidence indicate that senescent cells in the tumor microenvironment survive and develop a secretory profile composed mainly of inflammatory cytokines. This phenomenon is called the senescence-associated secretory phenotype (SASP) (Coppé et al., 2008; Gorgoulis et al., 2019), which enhances the proliferation and invasion of the surrounding cancer cells; in addition, this phenomenon promotes angiogenesis by recruiting macrophages and enhances the immunosuppressive microenvironment in a context-dependent manner (Kelly et al., 2007; Ruhland et al., 2016; Lee and Schmitt, 2019).

In contrast to the SASP as a chronic event, an acute stress-associated phenotype (ASAP) before the appearance of senescence markers is recognized as the rapid cellular response to various stresses, such as treatment by cytotoxic agents (Gilbert and Hemann, 2010). Although the transition from an ASAP to a chronic SASP has remained an intriguing topic, little is known about the mechanism. Chronic inflammation is deeply implicated in cellular senescence (Jurk et al., 2014). Moreover, inflammasome-mediated IL-1 signaling controls the SASP (Acosta et al., 2013), suggesting that cancer-related inflammation could be involved in the transition from an ASAP to a SASP. The present study was conducted to investigate the molecular mechanism of the transition during cancer-related inflammation and to reveal the role of senescent non-malignant cells in the metastatic process in GC patients.

RESULTS

CAFs influenced by pro-inflammatory cytokines tend to shift to the senescent state through the activation of nuclear factor κB (NF-κB) signaling

We isolated primary fibroblasts, CAFs, and normal fibroblasts (NFs) from resected tissues from GC patients and cultured the primary fibroblasts *in vitro*. These primary fibroblasts (NFs and CAFs) were confirmed to express the primary fibroblast marker CD90 by flow cytometry and to express four representative genes (*RHBDF2*, *IL7R*, *CADM1*, and *TM4SF1*) that are highly expressed in CAFs according to the RNA sequencing data in our previous study (Ishimoto et al., 2017) (Figures S1A and S1B). Based on our observations, we found that CAFs grew slower than NFs. Thus, we first examined the growth rate of NFs and CAFs at the same number of passages after isolation and showed that the growth rate of NFs was higher than that of CAFs (Figure 1A). We next examined the expression of $p16^{INK4a}$ (p16) and $p15^{INK4b}$ (p15), which are implicated in cell-cycle regulation and cellular senescence, via western blot (WB) analysis of NFs and CAFs at the same passage number. However, the expression of these proteins was hardly detected and was almost the same for both NFs and CAFs (Figure 1B). We also compared the telomere length using six NFs genomic DNA samples from paired NFs and CAFs at the same passage number. Although the length of the telomeres in NFs had a tendency to be slightly longer than that in CAFs, the average telomere length in NFs was not significantly different from that in CAFs (Figure 1C). These modest differences may be explained by epigenetic alterations in NFs during chronic inflammation caused by *H. pylori* infection (Maeda et al., 2020).

As shown in our previous study, three inflammatory cytokines (3CKs), interleukin-1α (IL-1α), (IL-1β), and tumor necrosis factor α (TNF-α), endow NFs with a CAF-like morphology, and high expression of 3CKs in GC tissues was significantly associated with a poor prognosis for patients with GC, although the expression level of each individual cytokine was not associated with the

Figure 1. CAFs stimulated with proinflammatory cytokines undergo a shift in the senescence status through the activation of NF-κB signaling

(A) Growth assay of 6 NFs and CAFs at the same passage number incubated for 4 days (**$p < 0.01$, $n = 6$).

(B) WB analysis of p16 and p15 in 3 NFs and CAFs at the same passage number (3). β-Actin was similarly analyzed as a loading control.

(C) Telomere length of 6 pairs of NFs and CAFs. The dot plots show the telomere length.

(D) Growth assay of 3 NFs for 3 days after treatment with 3CKs (**$p < 0.01$; n.s., not significant, $n = 3$).

(E) Growth assay of 3 CAFs for 3 days after treatment with 3CKs (*$p < 0.05$ and **$p < 0.01$; $n = 3$).

(F) WB analysis of p16, p15, and Lamin B1 in NFs, untreated or treated with 3CKs. β-Actin was similarly analyzed as a loading control.

(G) WB analysis of p16, p15, and Lamin B1 in CAFs, untreated or treated with 3CKs. β-Actin was similarly analyzed as a loading control.

(H) SA-β-gal staining of the control (3CKs(−) day 0), cultivated for 7 days with conditioned medium without passaging (3CKs(−) day 7), and cultivated for 7 days after treatment with 3CKs (3CKs(+) day 7). Scale bars, 300 μm. The graph shows the percentage of SA-β-gal$^+$ cells. At least 100 cells were counted in each group (*$p < 0.05$ and **$p < 0.01$; $n = 3$).

(I) Growth assay of 3 CAF lines treated with or without 3CKs for 10 days (**$p < 0.01$, $n = 3$).

(J) Immunofluorescence staining for markers of γH2AX and phospho-Ser/Thr ATM/ATR (pST/Q) substrate together with nuclear staining with DAPI in CAFs 5 days after the 3CK treatment; long-term passaged CAFs served as a positive control. The graph shows the percentage of nuclei that contain double-positive staining for both γH2AX and pST/Q. At least 100 cells were counted in each group (**$p < 0.01$, $n = 3$).

(K) WB analysis of NF-κB (p65) in 3 CAF lines treated with or without 3CKs. α-Tubulin was similarly analyzed as a loading control for cytoplasmic proteins, and histone 3 (H3) was similarly analyzed as a loading control for nuclear proteins.

(L) Immunofluorescence staining for NF-κB together with nuclear staining with DAPI in CAFs treated with or without 3CKs. Scale bars, 50 μm.

prognosis of patients with GC (Ishimoto et al., 2017). Based on these findings, we investigated the effects of 3CKs on CAFs and NFs according to the protocol (Figure S1C). We examined the morphological differences in the responses to 3CKs between NFs and CAFs and found that both NFs and CAFs treated with 3CKs showed similar spindle-shaped cell bodies, unlike the control (Figure S1D). However, the growth rate of CAFs was much more strongly suppressed by 3CK stimulation than was that of NFs (Figures 1D and 1E). Subsequently, WB analysis showed that 3CKs markedly increased the expression of p16 and p15 and decreased the expression of Lamin B1, as senescence markers, in CAFs compared with NFs (Figures 1F and 1G). These results implied that CAFs are likely to shift to a senescent state under exposure to 3CKs. In addition, senescence-associated β-galactosidase (SA-β-gal) staining was conducted to detect senescent cells, and the population of SA-β-gal$^+$ senescent cells was markedly increased in CAFs treated with 3CKs (Figure 1H). We performed the growth assay over a long period and assessed the DNA damage response, which is known to be a characteristic of senescent cells, to further examine whether 3CK stimulation induces irreversible cellular senescence. Consequently, growth arrest was induced in three independent CAF lines treated with 3CKs, and γH2A histone family member X (γH2AX) and phosphorylation of the consensus target sequences (pST/Q) accumulated in CAFs treated with 3CKs and in senescent CAFs induced by long-term passaging (Figures 1I and 1J) (Takahashi et al., 2017).

Several studies have demonstrated that NF-κB transcription factors are involved in senescence (Salminen et al., 2012). In general, the pro-inflammatory cytokines IL-1α, IL-1β, and TNF-α, are known to be upstream of NF-κB signaling. Thus, we conducted WB analyses and immunofluorescence staining to examine the nuclear translocation of p65 and confirmed the translocation in CAFs treated with 3CKs (Figures 1K and 1L). Moreover, we conducted an NF-κB loss-of-function study using NF-κB (p65) small interfering RNA (siRNA) to show the importance of NF-κB signaling in the senescent state in CAFs treated with 3CKs. The intracellular reactive oxygen species (ROS) level has been shown to cause DNA damage and induce cell-cycle arrest in oncogene-induced senescence (Kuilman et al., 2008; Takahashi et al., 2018). We showed that NF-κB (p65) knockdown significantly decreased the intracellular ROS level and the accumulation of γH2AX and pST/Q in CAFs treated with 3CKs (Figures S2A–S2C). These findings strongly support the hypothesis that activated NF-κB signaling leads to cellular senescence in CAFs treated with 3CKs.

Depletion of H3K27me3 marks by EZH2 downregulation leads to the maintenance of SASP factors in S-CAFs

To further examine the changes in the molecular profile in CAFs treated with 3CKs, we conducted comprehensive gene expression analysis by RNA sequencing. In addition, the gene set enrichment analysis (GSEA) of RNA sequencing data revealed that NF-κB target and senescence-related gene sets were enriched in CAFs treated with 3CKs compared with control CAFs (Figures 2A and 2B). Because NF-κB signaling is a major inducer of the SASP (Salminen et al., 2012), we next examined whether senescent CAFs induced by the 3CK treatment, defined as S-CAFs, exhibit the SASP. RNA sequencing data revealed that the expression of 21 genes previously reported as SASP factors (Prime et al., 2017) was strongly induced in S-CAFs treated with 3CKs (Figure 2C). We next confirmed the induction of major SASP factors by qRT-PCR (Figure 2D). NF-κB (p65) knockdown also significantly decreased the expression of SASP factors (Figure S2D). We examined the expression of 6 SASP factors 7 days after 3CK treatment to further assess whether this induction is an acute response mediated by the activation of NF-κB signaling and notably found that the induced expression of these factors was maintained at high levels for 7 days (Figure S3A). The expression of these SASP factors in S-CAFs treated with 3CKs was substantially higher than in untreated CAFs after long-term passaging (Figures S3B and S3C).

Some Polycomb group (PcG) proteins are downregulated, leading to the loss of trimethylation of lysine 27 on histone H3 (H3K27me3) at the CDKN2A locus, which results in the upregulation of p16 during senescence (Bracken et al., 2007). One of the PcG components, EZH2, is the histone lysine methyltransferase that catalyzes the H3K27me3. The inhibition of EZH2 activity induces senescence in the absence of DNA damage by depleting H3K27me3 marks and activating the p16 and SASP genes (Ito et al., 2018). This led us to hypothesize that the loss of the H3K27me3 marks by EZH2 downregulation may lead to the maintenance of SASP factors in S-CAFs by 3CK treatment. To address this hypothesis, we examined the time course of the p16, EZH2, and H3K27me3 marks. The WB analysis showed decreased expression of EZH2 and increased levels of p16 five days after the 3CK treatment; in addition, H3K27me3 marks were depleted within 7 days after 3CK treatment (Figure 2E). EZH2-overexpressing CAFs were generated and the H3K27me3 status was examined after treatment with 3CKs to further examine the importance of EZH2 downregulation in the maintenance of SASP factors in S-CAFs treated with 3CKs. The level of H3K27me3 marks was maintained, and the expression of p16 was not increased in EZH2-overexpressing CAFs 7 days after the 3CK treatment (Figure 2F). Notably, the expression levels of SASP factors were significantly decreased in EZH2-overexpressing CAFs compared with mock transfected CAFs 7 days after the 3CK treatment (Figure 2G). Moreover, the chromatin immunoprecipitation (ChIP) sequencing analysis revealed a marked decrease in the H3K27me3 modification at the promoter region of SASP factors in CAFs treated with 3CKs, whereas the modifications were not changed in EZH2-overexpressing CAFs treated with 3CKs (Figures 2H and 2I). Based on these results, the demethylation of H3K27me3 marks induced by EZH2 downregulation plays a crucial role in the maintenance of SASP factors in S-CAFs.

S-CAFs enhance GC cell growth through Janus kinase/signal transducer and activator of transcription 3 (JAK/STAT3) signaling

SASP factors are commonly considered to enhance cancer progression (Coppé et al., 2008; Yoshimoto et al., 2013). Thus, we examined the growth of the GC cell lines OCUM-2MD3 and NUGC3 treated with the conditioned medium (CM) of CAFs (CAF-CM) or S-CAFs (S-CAF-CM). Compared with the growth of GC cells treated with normal medium

CellPress
OPEN ACCESS

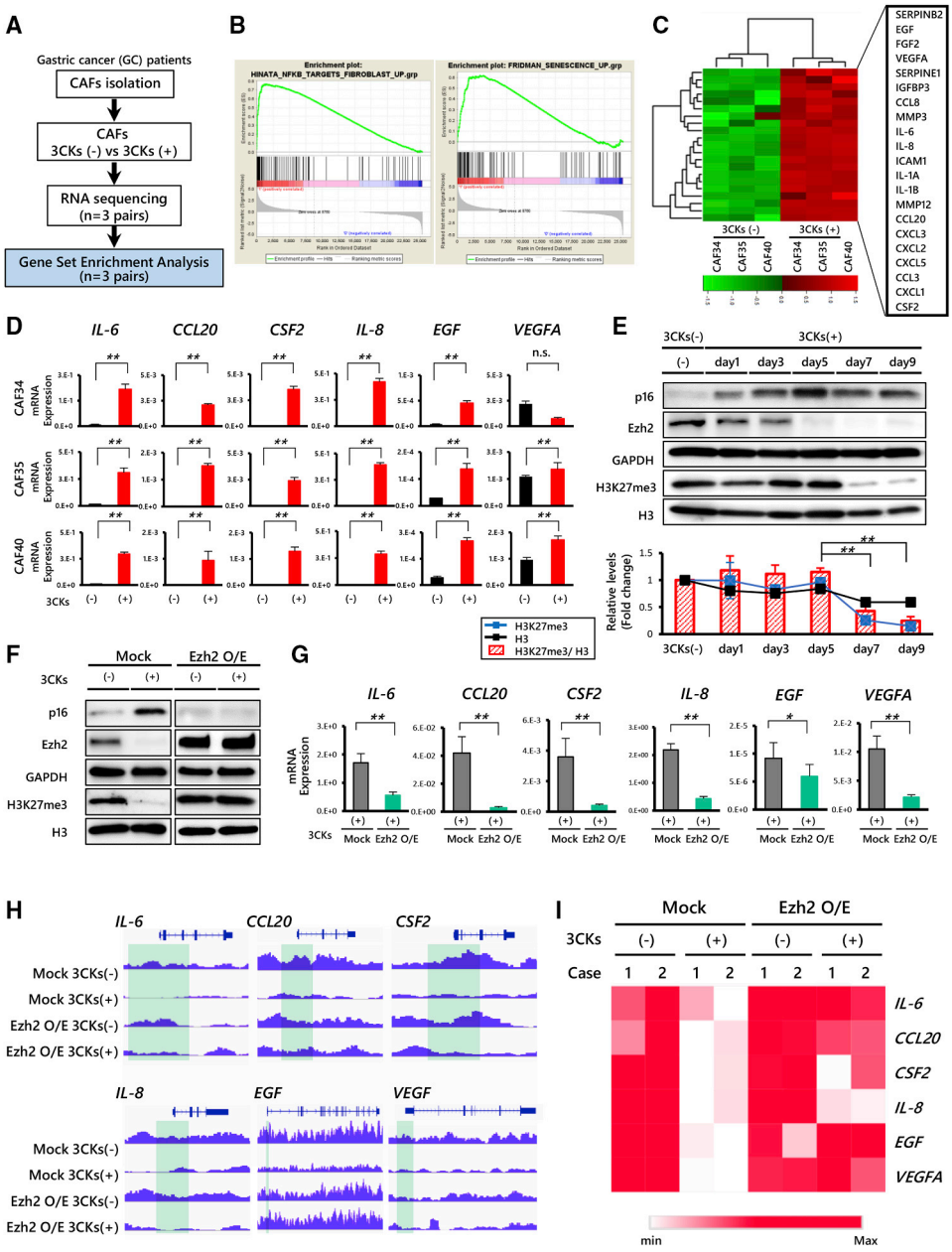

Figure 2. Depletion of H3K27me3 marks by EZH2 downregulation leads to maintenance of the SASP in CAFs

(A) Workflow of the genomic analysis conducted to examine the senescent state of CAFs treated with 3CKs.

(B) GSEA graphs for the upregulated signatures of NF-κB-related genes and senescence-related genes in 3 CAF lines 3 days after the 3CK treatment.

(C) Heatmap showing differentially expressed genes in 3 CAF lines 3 days after the 3CK treatment. A total of 21 uniquely expressed SASP-related genes for CAFs treated with 3CKs are indicated in the boxes.

(D) SASP factors that were upregulated by 3CKs, as validated by qRT-PCR (**$p < 0.01$; n.s., not significant, $n = 3$).

(E) WB analysis of p16, EZH2, and H3K27me3 levels in CAFs at the indicated time points after 3CK treatment. Glyceraldehyde 3-phosphate dehydrogenase (GAPDH) and H3 were similarly analyzed as loading controls. Graph shows the normalization of the H3K27me3 level to the total H3 level in WB analysis (**$p < 0.01$, $n = 3$).

(F and G) CAFs were transfected with an empty vector (mock) or EZH2 overexpression vector and then treated with or without 3CKs. Each of the 4 groups was evaluated 7 days after the 3CK or control treatment. WB analysis of p16, EZH2, and H3K27me3 levels in each of the 4 groups. GAPDH and H3 levels were similarly analyzed as loading controls (F). SASP factors analyzed using qRT-PCR in each 3CK treatment group (*$p < 0.05$ and **$p < 0.01$; $n = 3$) (G).

(H) Representative for duplicate ChIP sequencing (seq) data for SASP gene loci in each group.

(I) Heatmap quantifying the highlighted area, where the signal intensities are located ±2 kb from the transcription start site in the promoter regions of SASP genes in duplicate data.

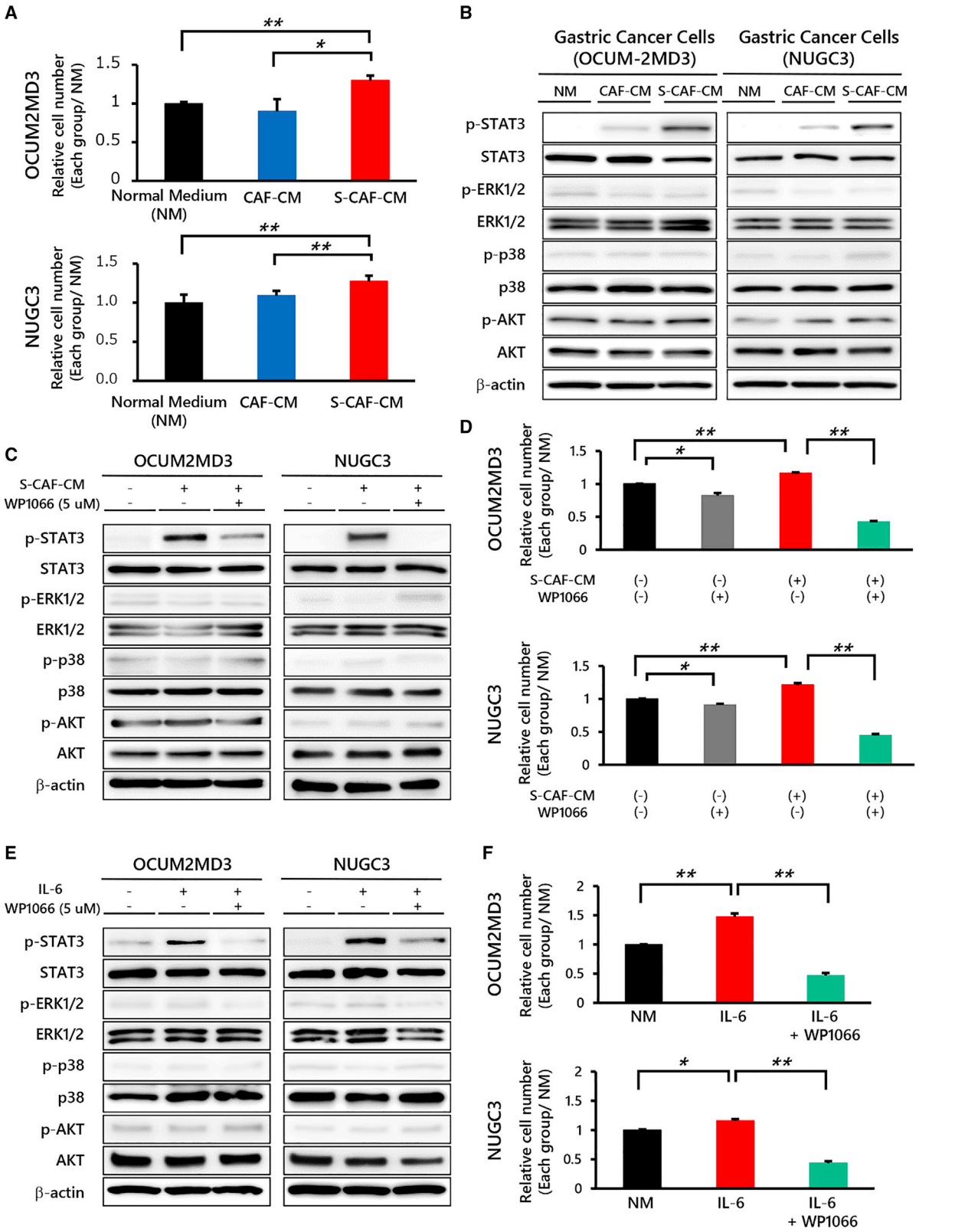

(legend on next page)

(NM) and CAF-CM, the growth of GC cells treated with S-CAF-CM was significantly increased (Figure 3A). We examined the status of various kinases using WB analysis to verify which signaling pathway was involved in the enhanced growth of GC cells treated with S-CAFs and observed a substantial increase in the phosphorylation of STAT3 in cells treated with S-CAF-CM (Figure 3B). Moreover, we investigated the importance of p-STAT3 activation in GC cell growth enhanced by S-CAFs using STAT3 knockdown by specific siRNA and WP1066, a potent inhibitor of the JAK/STAT3 pathway (Kong et al., 2008). We examined the viability of OCUM-2MD3 and NUGC3 cells treated with various concentrations of WP1066 and found that 5 μM WP1066 effectively blocked JAK/STAT3 activation by S-CAF without cytotoxicity (Figures 3C and S4A). Notably, WP1066 more effectively suppressed the viability of GC cells treated with S-CAF-CM than GC cells without S-CAF-CM (Figure S4B) and remarkably decreased the number of GC cells treated with S-CAF-CM compared with GC cells without S-CAF-CM (Figure 3D). Similarly, STAT3 knockdown significantly decreased the number of GC cells treated with S-CAF-CM (Figures S4C–S4F). These findings imply that the growth of GC cells treated with S-CAF-CM depends on JAK/STAT3 signaling and that blockade by WP1066 leads to reductions in GC cell viability and growth. In addition, the growth of GC cells treated with recombinant IL-6 was significantly increased, and WP1066 effectively blocked JAK/STAT3 pathway activation and reduced the number of GC cells in the group treated with recombinant IL-6 (Figures 3E and 3F). These findings suggest that among the SASP factors, IL-6 has a prominent effect on GC cell growth.

GC patients with peritoneal dissemination show systemic inflammation, and ascites from these patients contains p16$^+$ fibroblasts that highly express SASP factors

We compared serum levels of C-reactive protein (CRP), an inflammatory marker, the proportion of neutrophils, and the number of white blood cells in patients with early and advanced GC presenting without or with peritoneal dissemination to determine the stage at which CAFs were affected by inflammatory cytokines during the process of GC progression. Intriguingly, significantly higher serum CRP levels and proportions of neutrophils were detected in patients with GC presenting with peritoneal dissemination than in the other groups (Figure 4A). This result suggests that systemic inflammation occurs in GC patients with peritoneal dissemination. Given this finding, we presumed that the fibroblasts in the ascites of GC patients with peritoneal dissemination contain a senescent population exhibiting the SASP. We isolated CD90$^+$/platelet-derived growth factor receptor α^+ (PDGFRα^+) mesenchymal cells, including fibroblasts, epithelial cell adhesion molecule-positive (EpCAM$^+$) cancer cells, and CD45$^+$ hematopoietic cells, from the ascites of patients with GC (Figures 4B and S5A) and examined the expression of SASP factors to investigate this possibility. Notably, all SASP factors were expressed at higher levels in CD90$^+$/PDGFRα^+ fibroblasts than in the other populations (Figure 4C). Moreover, we performed single-cell mass cytometry (CyTOF) using ascites from 5 patients with GC presenting peritoneal dissemination and the ascites of 2 patients with liver cirrhosis (LC) as a control, and found that p16-high fibroblasts were more frequently detected in the ascites from patients with GC than in the ascites from patients with LC (Figure 4D). Further analysis of the ascites from patients with GC revealed significantly higher expression of p16 and IL-6 in fibroblasts than in the other cell populations (Figure 4E). In addition, we compared the IL-6 expression level between p16-high and p16-low fibroblasts and detected significantly higher expression in p16-high fibroblasts than in p16-low fibroblasts derived from the ascites from patients with GC (Figures 4F and S5B). These findings suggest that p16$^+$ fibroblasts exist in the ascites of GC patients with peritoneal dissemination and exhibit the SASP.

S-CAFs enhance peritoneal tumor formation through JAK/STAT3 signaling *in vivo*

Based on the above findings, we conducted peritoneal dissemination model experiments using OCUM-2MD3 cells to evaluate the role of S-CAFs in the development of peritoneal dissemination *in vivo*. The peritoneal tumors of OCUM-2MD3-inoculated mice treated with S-CAF-CM for 30 days were significantly larger than tumors from the other two groups, and weight loss was not observed (Figures 5A and S6A). In addition, the serum CRP levels indicating systemic inflammation were also significantly increased in OCUM-2MD3-inoculated mice treated with S-CAF-CM (Figure 5B). We further assessed the p-STAT3 levels in tumors in these 3 groups by WB analysis and immunohistochemical (IHC) staining. The tumor cells from the OCUM-2MD3-inoculated mice treated with S-CAF-CM showed higher p-STAT3 levels than the mice in the other 2 groups (Figures 5C–5E). Supporting the findings from previous reports indicating that STAT-3 activation induces the expression of antiapoptotic proteins (Bhattacharya et al., 2005), Bcl-2 expression was increased in the tumors of the

Figure 3. JAK/STAT3 signaling activation by S-CAFs enhances GC cell growth

(A) Growth assay of OCUM-2MD3 and NUGC3 cells, untreated and treated with CAF-CM or S-CAF-CM for 3 days. We collected S-CAF-CM from S-CAFs induced by 3CKs (*$p < 0.05$ and **$p < 0.01$; n = 3).

(B) WB analysis of p-STAT3, p-ERK1/2, p-p38, and p-AKT levels in OCUM-2MD3 and NUGC3 cells. Cells were untreated and treated with CAF-CM or S-CAF-CM for 10 min.

(C) WB analysis of p-STAT3, p-ERK1/2, p-p38, and p-AKT levels in OCUM-2MD3 and NUGC3 cells treated with S-CAF-CM, vehicle (DMSO), or WP1066 for 120 min.

(D) Growth assays of OCUM-2MD3 and NUGC3 cells treated with S-CAF-CM, vehicle (DMSO), or WP1066 for 3 days (*$p < 0.05$ and **$p < 0.01$; n = 3).

(E) WB analysis of p-STAT3, p-ERK1/2, p-p38, and p-AKT levels in OCUM-2MD3 and NUGC3 cells treated with IL-6, vehicle (DMSO), or WP1066 for 120 min.

(F) Growth assays of OCUM-2MD3 and NUGC3 cells treated with IL-6, vehicle (DMSO), or WP1066 for 3 days (*$p < 0.05$ and **$p < 0.01$; n = 3).

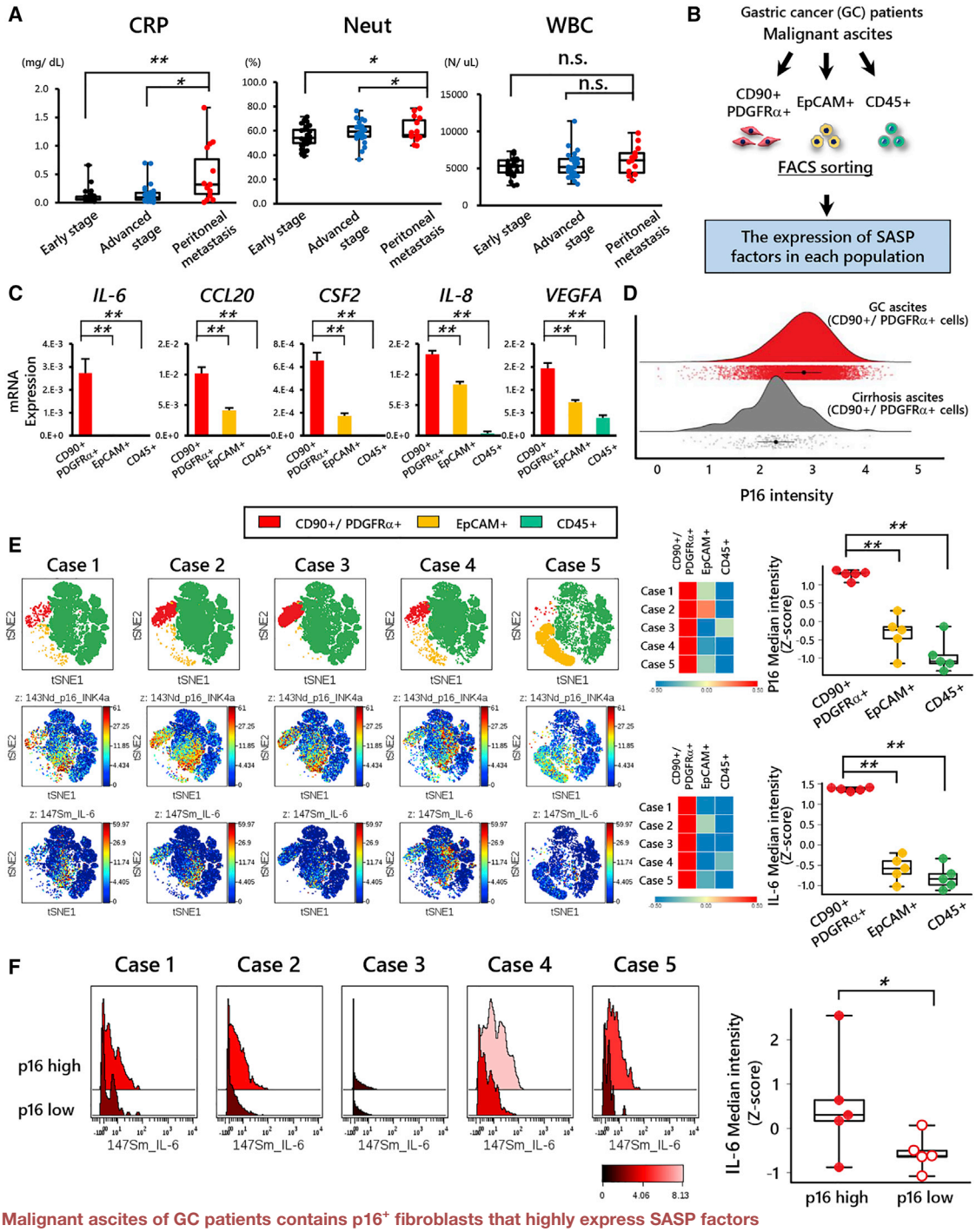

Figure 4. Malignant ascites of GC patients contains p16$^+$ fibroblasts that highly express SASP factors

(A) Serum levels of CRP, white blood cells (WBCs), and the proportion of neutrophils in early GC patients and advanced GC patients with or without peritoneal dissemination (*$p < 0.05$ and **$p < 0.01$; n.s., not significant, early GC patients, n = 30; advanced GC patients without peritoneal dissemination, n = 30; and advanced GC patients with peritoneal dissemination, n = 15).

(B) Workflow of sorting 100 cells of each labeled population (CD90/platelet-derived growth factor receptor α [PDGFR-α], EpCAM, and CD45) and collection of their mRNA from GC patients with ascites.

(C) SASP factors of each population validated by qRT-PCR (**$p < 0.01$; n = 3).

(D) Histograms represent the arcsinh-transformed p16 expression normalized to a 0–5 range between the GC malignant ascites and cirrhosis ascites groups.

(E) t-SNE plots with labeled populations (CD90/PDGFR-α, EpCAM, and CD45) and heatmap showing the intensity of p16 and IL-6. Colors show row-normalized *Z* score of gene expression values. The graph shows the quantification of the expression levels of p16 and IL-6 (**$p < 0.01$; n = 5).

(F) Histograms represent the expression of IL-6 between the p16-high and p16-low groups. The graph shows the quantification of the expression level of IL-6 in each group (*$p < 0.05$; n = 5).

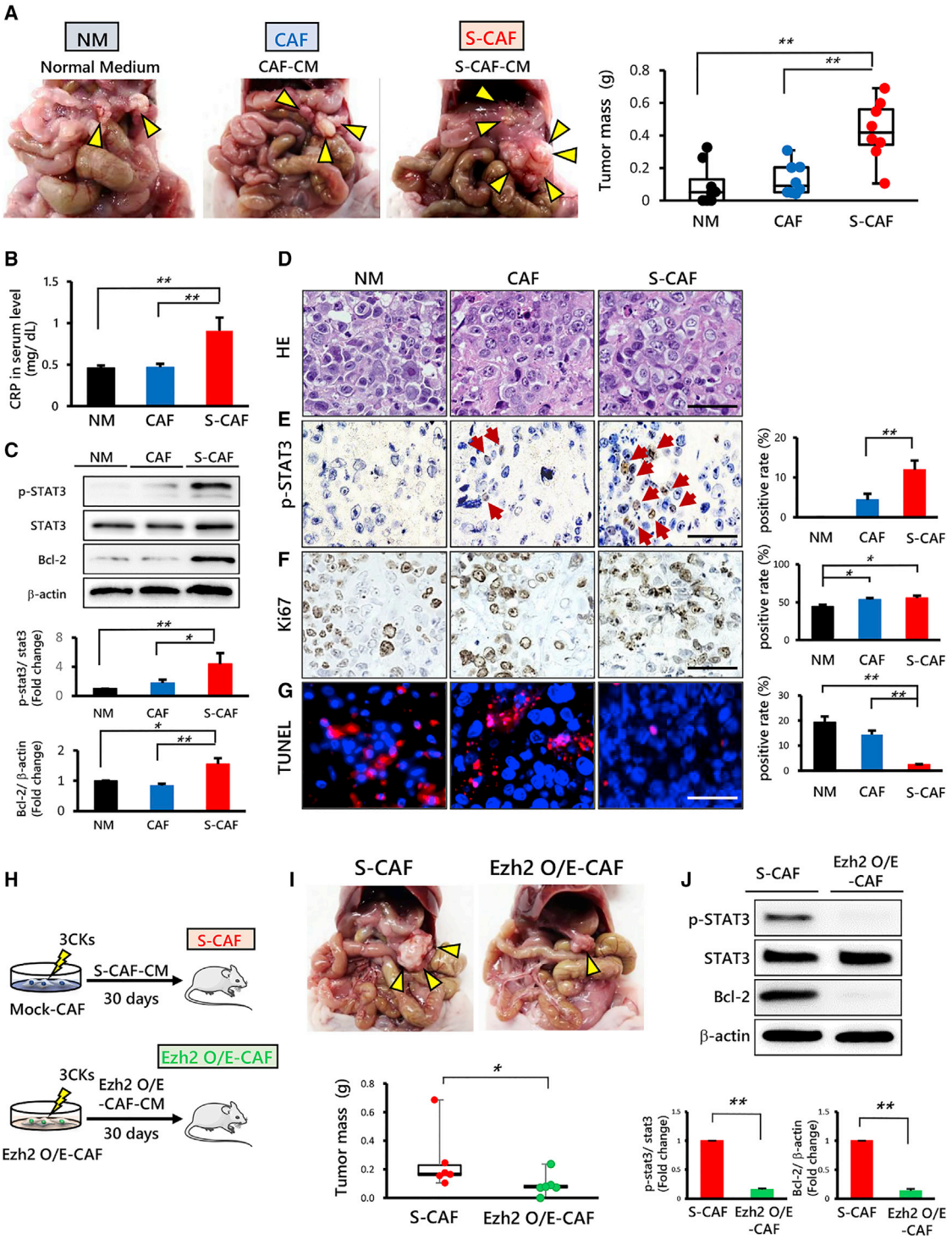

Figure 5. JAK/STAT3 signaling activation by S-CAF enhances peritoneal tumor formation

(A) Representative images of OCUM-2MD3-bearing mice after daily intraperitoneal injections of CAF-CM, S-CAF-CM, or normal medium. The graph shows the quantification of the tumor masses of each group (day 30) (**$p < 0.01$; n = 8).

(B) ELISA of CRP in the serum of each group of OCUM-2MD3-bearing mice (**$p < 0.01$; n = 3).

(C) WB analysis of p-STAT3 and Bcl-2 in the implanted OCUM-2MD3 cells of each group. The graph shows the normalization of p-STAT3 to total STAT3 and the normalization of Bcl-2 to total β-actin (*$p < 0.05$ and **$p < 0.01$; n = 3).

(legend continued on next page)

OCUM-2MD3-inoculated mice treated with S-CAF-CM (Figure 5C). Moreover, Ki67 and terminal deoxynucleotidyl transferase dUTP nick end labeling (TUNEL) staining showed significantly higher viability of the tumor cells in the S-CAF-CM group than in the other 2 groups (Figures 5F and 5G). In addition, the peritoneal tumors of OCUM-2MD3-inoculated mice treated with recombinant IL-6 for 30 days were larger and displayed apoptosis inhibition and significantly higher p-STAT3 and Bcl-2 levels than tumors from mice in the control group (Figures S6B–S6E). Together with the results of the *in vitro* experiments, these findings suggest that among the SASP factors, IL-6 enhances peritoneal tumor formation through JAK/STAT3 signaling.

Because the expression levels of SASP factors were significantly decreased in EZH2-overexpressing CAFs treated with 3CKs (Figure 2G), we next examined the effect of S-CAFs mediated by EZH2 downregulation on peritoneal tumor formation. The volumes of peritoneal tumors in the EZH2 O/E-CAF-CM group were significantly smaller than the S-CAF-CM group, and weight loss was not observed (Figures 5H, 5I, and S6F). Moreover, p-STAT3 and Bcl-2 levels in the tumor lysates of the EZH2 O/E-CAF-CM group were markedly decreased compared with the S-CAF-CM group (Figure 5J). These results indicate that S-CAFs mediated by EZH2 downregulation activate JAK/STAT3 signaling and promote peritoneal tumor formation by inhibiting apoptosis.

A JAK/STAT3 inhibitor effectively blocks the increase in peritoneal tumor formation induced by S-CAFs *in vivo*

Finally, the OCUM-2MD3-inoculated mice treated with S-CAF-CM were additionally administered WP1066 according to the protocol (Figure 6A) to determine the therapeutic effect of the JAK/STAT3 inhibitor *in vivo*. Although the WP1066 treatment did not affect peritoneal tumor formation in mice that were not treated with S-CAF-CM (Figures S7A–S7C), the volumes of peritoneal tumors in the S-CAF-CM + WP1066 treatment group were significantly smaller than in the S-CAF-CM group, without weight loss (Figures 6B, S7D, and S7E). We next compared the p-STAT3 levels in the tumors between the 2 groups by WB analysis and IHC staining. Tumor cells in mice administered WP1066 showed lower p-STAT3 and Bcl-2 levels than those in S-CAF-CM-treated mice (Figures 6C–6E). Moreover, Ki67 and TUNEL staining revealed significantly lower viability of tumor cells in the mice treated with WP1066 than tumor cells in the S-CAF-CM-treated mice (Figures 6F and 6G). These results suggest that JAK/STAT3 signaling plays critical roles in the S-CAF-enhanced anti-apoptosis function and in peritoneal tumor formation *in vivo*.

DISCUSSION

Nonmalignant cells in the tumor microenvironment secrete various growth factors, cytokines, and microvesicles, which leads to the exacerbation of cancer in multiple processes (Bu et al., 2019). Previous evidence has indicated that senescent non-malignant cells exhibiting the SASP are induced by various stresses, such as ROS, and promote cancer development. Moreover, the anticancer drug-induced genotoxicity of nonmalignant cells may alter the tumor microenvironment, causing cellular senescence and drug resistance (Sun et al., 2012; Demaria et al., 2017). TAK1 increases the expression of zinc finger and SCAN domain containing 4 (Zscan4), a zinc finger transcription factor, and activates p38 and phosphatidylinositol 3-kinase/AKT/mammalian target of rapamycin (PI3K/AKT/mTOR) signaling to support persistent SASP signaling induced by cytotoxic agents (Zhang et al., 2018). Investigations using endothelial cells (ECs) have demonstrated that ECs damaged by anticancer drugs exhibit an ASAP as a rapid response to stress and are mechanistically distinct from the SASP (Gilbert and Hemann, 2010, 2011). Genotoxic damage signals are transmitted through master regulators such as NF-κB, and this results in a diverse secretory program that generates a proangiogenic, proinflammatory microenvironment (Sun and Nelson, 2012). We have now demonstrated the mechanism of transition from an acute inflammatory response to a SASP through NF-κB signaling activated by inflammatory cytokines in CAFs. Specifically, inflammatory cytokines induced the acute inflammatory response through the transient activation of NF-κB signaling and subsequent depletion of the H3K27me3 marks by EZH2 downregulation and led to the maintenance of SASP factors in S-CAFs. The current finding delineates one of the molecular mechanisms underlying the loss of H3K27me3, which is a distinct change in CAFs, and epigenetic change is involved in the tumor-promoting capacities of CAFs through the secretion of multiple stem cell niche factors (Maeda et al., 2020).

Senescent hepatic stellate cells promote obesity-associated hepatocellular carcinoma (HCC) development in mice by increasing the levels of deoxycholic acid produced by gut bacteria (Yoshimoto et al., 2013). Senescent CAFs secrete excessive amounts of IL-8 and promote pancreatic ductal adenocarcinoma (PDAC) invasion and metastasis, whereas an inhibitor of the IL-8 receptor blocked the motility of PDAC cells (Wang et al., 2017). In addition, IL-6 production in the tumor microenvironment leads to the activation of JAK/STAT3 signaling in both tumor cells and tumor-infiltrating immune cells, which can promote cancer progression (Johnson et al., 2018), and IL-6, among the SASP factors derived from senescent cells, causes chemoresistance in several kinds of tumors (Bent et al., 2016; Canino et al., 2012). Our current findings demonstrated that S-CAFs exhibiting the SASP promote peritoneal tumor formation through JAK/STAT3 signaling in a mouse model. Moreover, we showed the existence of fibroblasts harboring the characteristics of the SASP in the

(D–G) H&E staining (D) and IHC staining for p-STAT3 (E) and Ki67 (F) and immunofluorescence for TUNEL analysis (G) in the implanted OCUM-2MD3 cells of each group. Scale bars, 100 μm. Each graph shows the quantification of the positive rate. At least 100 cells were counted in each group (*$p < 0.05$ and **$p < 0.01$; $n = 3$).
(H) Schematic illustrating the experimental procedure (S-CAF, $n = 6$; EZH2 O/E-CAF, $n = 6$).
(I) Representative images of OCUM-2MD3-bearing mice treated daily with injections of S-CAF-CM (CAFs transfected with empty vector) or EZH2-overexpressing (EZH2 O/E)-CAFs-CM. The graph shows the quantification of the tumor masses in each group (*$p < 0.05$; $n = 6$).
(J) WB analysis of p-STAT3 and Bcl-2 levels in implanted OCUM-2MD3 cells in each group. The graph shows the normalization of p-STAT3 to total STAT3 and the normalization of Bcl-2 to total β-actin (**$p < 0.01$; $n = 3$).

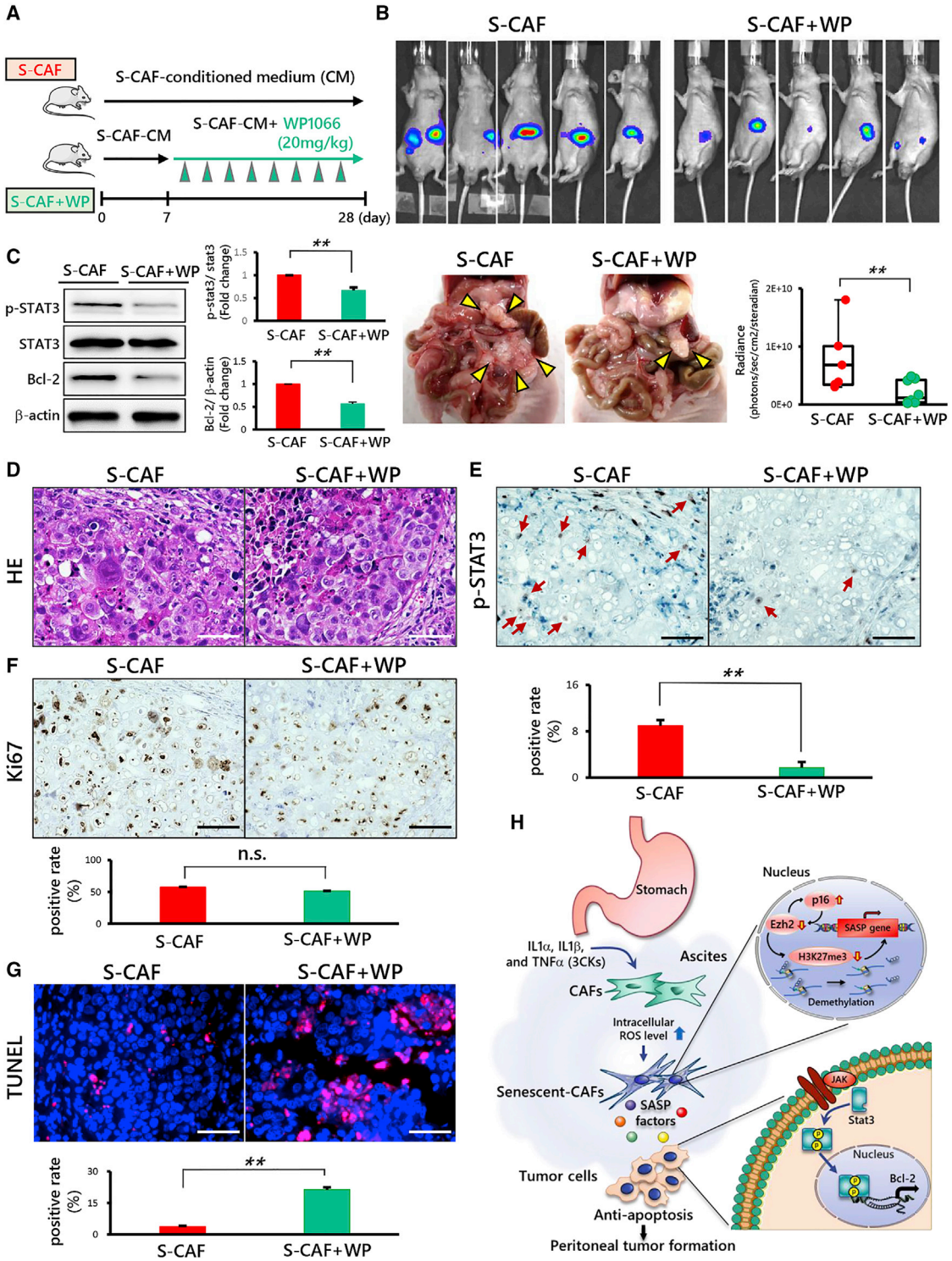

Figure 6. The JAK/STAT3 inhibitor effectively blocks the peritoneal tumor formation enhanced by S-CAFs

(A) Timeline of the experimental procedure (S-CAF, n = 6; S-CAF + WP, n = 8).

(B) *In vivo* imaging system (IVIS) images of OCUM-2MD3-bearing mice treated with daily S-CAF-CM injections and treated with vehicle (DMSO, control) or 20 mg/kg WP1066 a total of 8 times for 3 weeks. Representative images of each mouse group. The graph shows the quantification of the tumor sizes by *in vivo* luciferase assays (**p < 0.01; S-CAF, n = 6; S-CAF + WP, n = 8).

(legend continued on next page)

ascites of GC patients with peritoneal dissemination. Previous studies and the findings in the present article indicate that non-malignant cells exhibiting the SASP may enhance peritoneal dissemination and cancer progression in primary tumors.

Inflammation is a well-known hallmark of cancer that strongly contributes to the development and progression of malignancies (Hanahan and Weinberg, 2011). Systemic inflammation, similar to the local immune response, involves cytokines and small inflammatory proteins and immune cells; however, these mediators are detectable in the systemic circulation and give rise to the paraneoplastic symptoms observed in patients with cancer. Moreover, circulating cytokines, chemokines, and matrix-degrading proteins show similar functions in the systemic circulation and local tumor microenvironment and are crucial to the dissemination of tumors to distant sites (Diakos et al., 2014). In fact, we demonstrated that serum CRP levels and the proportion of neutrophils were significantly higher in GC patients with than in those without peritoneal dissemination. This finding implies that the local immune response in the peritoneal cavity associated with peritoneal dissemination causes systemic inflammation. Moreover, CRP is a member of the pentraxin family and is released by hepatocytes in response to proinflammatory cytokines, particularly IL-6 (Guthrie et al., 2013). Together with these previous studies, our present findings suggest that systemic inflammation in GC patients with peritoneal dissemination is enhanced by IL-6 derived from non-malignant cells in ascites.

In summary, the proinflammatory cytokines IL-1α, IL-1β, and TNF-α induce the activation of NF-κB signaling and cellular senescence by promoting ROS accumulation in CAFs. Subsequently, the expression of SASP factors, particularly IL-6, is maintained at a high level through the demethylation of H3K27me3 marks by EZH2 downregulation, resulting in enhanced peritoneal tumor formation through JAK/STAT3 signaling (Figure 6H). Given these findings, the disablement of fibroblasts harboring SASP in the ascites of GC patients with peritoneal dissemination may lead to the suppression of systemic inflammation and inhibition of subsequent peritoneal tumor formation.

STAR★METHODS

Detailed methods are provided in the online version of this paper and include the following:

SUPPLEMENTAL INFORMATION

Supplemental Information can be found online at https://doi.org/10.1016/j.celrep.2021.108779.

ACKNOWLEDGMENTS

The authors thank Y. Shiraishi (Radio Isotope Center, Institute of Resource Development and Analysis, Kumamoto University) for providing helpful advice on the use of the *in vivo* imaging system (Caliper IVIS Kinetic *In Vivo* Optical Imaging System), R. Koitabashi (International Research Center for Medical Sciences, Kumamoto University) for preparing cDNA samples from RT-RamDa, and S. Usuki (Liaison Laboratory Research Promotion Center, IMEG, Kumamoto University) for assisting with RNA sequencing and ChIP sequencing. This study was supported by the Japan Society for the Promotion of Science under grant nos. 16H06257, 18K08543, 20K08985, and 20H03531, the Mochida Memorial Foundation for Medical and Pharmaceutical Research, the MSD Life Science Foundation, the Public Interest Incorporated Foundation, and the Princess Takamatsu Cancer Research Fund.

AUTHOR CONTRIBUTIONS

Conception and design, T.Y., H.B., and T.I.; data acquisition, T.Y., M.K., A.Y., K. Miyake, R.K., S.K., T.Y.-N., and N.Y.-Y.; data analysis and interpretation (e.g., RNA sequencing, computational analysis), T.Y., M.K., A.Y., K. Miyake, S.K., K. Matsusaki, and T.I.; manuscript writing, review, and/or revision, T.Y., M.K., and T.I.; administrative, technical, or material support, T.U., R.I., L.B., L.F., K.A., D.I., S.I., K.E., M.I., Y.B., and N.Y.; study supervision, H.O., S.O., G.S., A.T., P.T., H.B., and T.I.

(C) WB analysis of p-STAT3 and Bcl-2 in the implanted OCUM-2MD3 cells of each group. Graphs show the normalization of p-STAT3 to total STAT3 and the normalization of Bcl-2 to total β-actin (**$p < 0.01$; $n = 3$).

(D–G) H&E staining (D) and IHC staining for p-STAT3 (E) and Ki67 (F) and immunofluorescence staining for TUNEL (G) in the implanted OCUM-2MD3 cells from each group. Scale bars, 100 μm. Each graph shows the quantification of the positive rate (**$p < 0.01$; n.s., not significant; $n = 3$).

(H) Schematic model of the enhancement of GC peritoneal tumor formation by S-CAFs exhibiting the SASP.

DECLARATION OF INTERESTS

The authors declare no competing interests.

Received: May 29, 2020
Revised: December 8, 2020
Accepted: February 2, 2021
Published: February 23, 2021

REFERENCES

Acosta, J.C., Banito, A., Wuestefeld, T., Georgilis, A., Janich, P., Morton, J.P., Athineos, D., Kang, T.W., Lasitschka, F., Andrulis, M., et al. (2013). A complex secretory program orchestrated by the inflammasome controls paracrine senescence. Nat. Cell Biol. *15*, 978–990.

Bent, E.H., Gilbert, L.A., and Hemann, M.T. (2016). A senescence secretory switch mediated by PI3K/AKT/mTOR activation controls chemoprotective endothelial secretory responses. Genes Dev. *30*, 1811–1821.

Bhattacharya, S., Ray, R.M., and Johnson, L.R. (2005). STAT3-mediated transcription of Bcl-2, Mcl-1 and c-IAP2 prevents apoptosis in polyamine-depleted cells. Biochem. J. *392*, 335–344.

Bracken, A.P., Kleine-Kohlbrecher, D., Dietrich, N., Pasini, D., Gargiulo, G., Beekman, C., Theilgaard-Mönch, K., Minucci, S., Porse, B.T., Marine, J.C., et al. (2007). The Polycomb group proteins bind throughout the INK4A-ARF locus and are disassociated in senescent cells. Genes Dev. *21*, 525–530.

Bray, F., Ferlay, J., Soerjomataram, I., Siegel, R.L., Torre, L.A., and Jemal, A. (2018). Global cancer statistics 2018: GLOBOCAN estimates of incidence and mortality worldwide for 36 cancers in 185 countries. CA Cancer J. Clin. *68*, 394–424.

Bu, L., Baba, H., Yoshida, N., Miyake, K., Yasuda, T., Uchihara, T., Tan, P., and Ishimoto, T. (2019). Biological heterogeneity and versatility of cancer-associated fibroblasts in the tumor microenvironment. Oncogene *38*, 4887–4901.

Canino, C., Mori, F., Cambria, A., Diamantini, A., Germoni, S., Alessandrini, G., Borsellino, G., Galati, R., Battistini, L., Blandino, R., et al. (2012). SASP mediates chemoresistance and tumor-initiating-activity of mesothelioma cells. Oncogene *31*, 3148–3163.

Chau, I., Norman, A.R., Cunningham, D., Waters, J.S., Oates, J., and Ross, P.J. (2004). Multivariate prognostic factor analysis in locally advanced and metastatic esophago-gastric cancer–pooled analysis from three multicenter, randomized, controlled trials using individual patient data. J. Clin. Oncol. *22*, 2395–2403.

Coppé, J.P., Patil, C.K., Rodier, F., Sun, Y., Muñoz, D.P., Goldstein, J., Nelson, P.S., Desprez, P.Y., and Campisi, J. (2008). Senescence-associated secretory phenotypes reveal cell-nonautonomous functions of oncogenic RAS and the p53 tumor suppressor. PLoS Biol. *6*, 2853–2868.

Demaria, M., O'Leary, M.N., Chang, J., Shao, L., Liu, S., Alimirah, F., Koenig, K., Le, C., Mitin, N., Deal, A.M., et al. (2017). Cellular Senescence Promotes Adverse Effects of Chemotherapy and Cancer Relapse. Cancer Discov. *7*, 165–176.

Diakos, C.I., Charles, K.A., McMillan, D.C., and Clarke, S.J. (2014). Cancer-related inflammation and treatment effectiveness. Lancet Oncol. *15*, e493–e503.

Gilbert, L.A., and Hemann, M.T. (2010). DNA damage-mediated induction of a chemoresistant niche. Cell *143*, 355–366.

Gilbert, L.A., and Hemann, M.T. (2011). Chemotherapeutic resistance: surviving stressful situations. Cancer Res. *71*, 5062–5066.

Gorgoulis, V., Adams, P.D., Alimonti, A., Bennett, D.C., Bischof, O., Bishop, C., Campisi, J., Collado, M., Evangelou, K., Ferbeyre, G., et al. (2019). Cellular Senescence: Defining a Path Forward. Cell *179*, 813–827.

Guthrie, G.J., Roxburgh, C.S., Horgan, P.G., and McMillan, D.C. (2013). Does interleukin-6 link explain the link between tumour necrosis, local and systemic inflammatory responses and outcome in patients with colorectal cancer? Cancer Treat. Rev. *39*, 89–96.

Hanahan, D., and Weinberg, R.A. (2011). Hallmarks of cancer: the next generation. Cell *144*, 646–674.

Ishimoto, T., Izumi, D., Watanabe, M., Yoshida, N., Hidaka, K., Miyake, K., Sugihara, H., Sawayama, H., Imamura, Y., Iwatsuki, M., et al. (2015). Chronic inflammation with Helicobacter pylori infection is implicated in CD44 overexpression through miR-328 suppression in the gastric mucosa. J. Gastroenterol. *50*, 751–757.

Ishimoto, T., Miyake, K., Nandi, T., Yashiro, M., Onishi, N., Huang, K.K., Lin, S.J., Kalpana, R., Tay, S.T., Suzuki, Y., et al. (2017). Activation of Transforming Growth Factor Beta 1 Signaling in Gastric Cancer-associated Fibroblasts Increases Their Motility, via Expression of Rhomboid 5 Homolog 2, and Ability to Induce Invasiveness of Gastric Cancer Cells. Gastroenterology *153*, 191–204.e16.

Ito, T., Teo, Y.V., Evans, S.A., Neretti, N., and Sedivy, J.M. (2018). Regulation of Cellular Senescence by Polycomb Chromatin Modifiers through Distinct DNA Damage- and Histone Methylation-Dependent Pathways. Cell Rep. *22*, 3480–3492.

Johnson, D.E., O'Keefe, R.A., and Grandis, J.R. (2018). Targeting the IL-6/JAK/STAT3 signalling axis in cancer. Nat. Rev. Clin. Oncol. *15*, 234–248.

Jurk, D., Wilson, C., Passos, J.F., Oakley, F., Correia-Melo, C., Greaves, L., Saretzki, G., Fox, C., Lawless, C., Anderson, R., et al. (2014). Chronic inflammation induces telomere dysfunction and accelerates ageing in mice. Nat. Commun. *2*, 4172.

Kalluri, R. (2016). The biology and function of fibroblasts in cancer. Nat. Rev. Cancer *16*, 582–598.

Kelly, J., Ali Khan, A., Yin, J., Ferguson, T.A., and Apte, R.S. (2007). Senescence regulates macrophage activation and angiogenic fate at sites of tissue injury in mice. J. Clin. Invest. *117*, 3421–3426.

Kong, L.Y., Abou-Ghazal, M.K., Wei, J., Chakraborty, A., Sun, W., Qiao, W., Fuller, G.N., Fokt, I., Grimm, E.A., Schmittling, R.J., et al. (2008). A novel inhibitor of signal transducers and activators of transcription 3 activation is efficacious against established central nervous system melanoma and inhibits regulatory T cells. Clin. Cancer Res. *14*, 5759–5768.

Kubota, S., Tokunaga, K., Umezu, T., Yokomizo-Nakano, T., Sun, Y., Oshima, M., Tan, K.T., Yang, H., Kanai, A., Iwanaga, E., et al. (2019). Lineage-specific RUNX2 super-enhancer activates MYC and promotes the development of blastic plasmacytoid dendritic cell neoplasm. Nat. Commun. *10*, 1653.

Kuilman, T., Michaloglou, C., Vredeveld, L.C., Douma, S., van Doorn, R., Desmet, C.J., Aarden, L.A., Mooi, W.J., and Peeper, D.S. (2008). Oncogene-induced senescence relayed by an interleukin-dependent inflammatory network. Cell *133*, 1019–1031.

Langmead, B., and Salzberg, S.L. (2012). Fast gapped-read alignment with Bowtie 2. Nat. Methods *9*, 357–359.

Lee, S., and Schmitt, C.A. (2019). The dynamic nature of senescence in cancer. Nat. Cell Biol. *21*, 94–101.

Maeda, M., Takeshima, H., Iida, N., Hattori, N., Yamashita, S., Moro, H., Yasukawa, Y., Nishiyama, K., Hashimoto, T., Sekine, S., et al. (2020). Cancer cell niche factors secreted from cancer-associated fibroblast by loss of H3K27me3. Gut *69*, 243–251.

Prime, S.S., Cirillo, N., Hassona, Y., Lambert, D.W., Paterson, I.C., Mellone, M., Thomas, G.J., James, E.N., and Parkinson, E.K. (2017). Fibroblast activation and senescence in oral cancer. J. Oral Pathol. Med. *46*, 82–88.

Quail, D.F., and Joyce, J.A. (2013). Microenvironmental regulation of tumor progression and metastasis. Nat. Med. *19*, 1423–1437.

Ruhland, M.K., Loza, A.J., Capietto, A.H., Luo, X., Knolhoff, B.L., Flanagan, K.C., Belt, B.A., Alspach, E., Leahy, K., Luo, J., et al. (2016). Stromal senescence establishes an immunosuppressive microenvironment that drives tumorigenesis. Nat. Commun. *7*, 11762.

Salminen, A., Kauppinen, A., and Kaarniranta, K. (2012). Emerging role of NF-κB signaling in the induction of senescence-associated secretory phenotype (SASP). Cell. Signal. *24*, 835–845.

Sun, Y., and Nelson, P.S. (2012). Molecular pathways: involving microenvironment damage responses in cancer therapy resistance. Clin. Cancer Res. *18*, 4019–4025.

Sun, Y., Campisi, J., Higano, C., Beer, T.M., Porter, P., Coleman, I., True, L., and Nelson, P.S. (2012). Treatment-induced damage to the tumor microenvironment promotes prostate cancer therapy resistance through WNT16B. Nat. Med. *18*, 1359–1368.

Takahashi, A., Okada, R., Nagao, K., Kawamata, Y., Hanyu, A., Yoshimoto, S., Takasugi, M., Watanabe, S., Kanemaki, M.T., Obuse, C., and Hara, E. (2017). Exosomes maintain cellular homeostasis by excreting harmful DNA from cells. Nat. Commun. *8*, 15287.

Takahashi, A., Loo, T.M., Okada, R., Kamachi, F., Watanabe, Y., Wakita, M., Watanabe, S., Kawamoto, S., Miyata, K., Barber, G.N., et al. (2018). Downregulation of cytoplasmic DNases is implicated in cytoplasmic DNA accumulation and SASP in senescent cells. Nat. Commun. *9*, 1249.

Thomassen, I., van Gestel, Y.R., van Ramshorst, B., Luyer, M.D., Bosscha, K., Nienhuijs, S.W., Lemmens, V.E., and de Hingh, I.H. (2014). Peritoneal carcinomatosis of gastric origin: a population-based study on incidence, survival and risk factors. Int. J. Cancer *134*, 622–628.

Ushijima, T., and Hattori, N. (2012). Molecular pathways: involvement of Helicobacter pylori-triggered inflammation in the formation of an epigenetic field defect, and its usefulness as cancer risk and exposure markers. Clin. Cancer Res. *18*, 923–929.

Van Gassen, S., Callebaut, B., Van Helden, M.J., Lambrecht, B.N., Demeester, P., Dhaene, T., and Saeys, Y. (2015). FlowSOM: using self-organizing maps for visualization and interpretation of cytometry data. Cytometry A *87*, 636–645.

Wang, T., Notta, F., Navab, R., Joseph, J., Ibrahimov, E., Xu, J., Zhu, C.Q., Borgida, A., Gallinger, S., and Tsao, M.S. (2017). Senescent Carcinoma-Associated Fibroblasts Upregulate IL8 to Enhance Prometastatic Phenotypes. Mol. Cancer Res. *15*, 3–14.

Yoshimoto, S., Loo, T.M., Atarashi, K., Kanda, H., Sato, S., Oyadomari, S., Iwakura, Y., Oshima, K., Morita, H., Hattori, M., et al. (2013). Obesity-induced gut microbial metabolite promotes liver cancer through senescence secretome. Nature *499*, 97–101.

Zhang, B., Fu, D., Xu, Q., Cong, X., Wu, C., Zhong, X., Ma, Y., Lv, Z., Chen, F., Han, L., et al. (2018). The senescence-associated secretory phenotype is potentiated by feedforward regulatory mechanisms involving Zscan4 and TAK1. Nat. Commun. *9*, 1723.

STAR★METHODS

KEY RESOURCES TABLE

REAGENT or RESOURCE	SOURCE	IDENTIFIER
Antibodies		
Alexa Fluor 488 Goat anti-rabbit IgG	Molecular Probes	Cat# A11008; RRID: AB_143165
Alexa Fluor 594 Goat anti-mouse IgG	Molecular Probes	Cat# A11005; RRID: AB_2758358
Anti-human CD11b(Mac-1)	Fluidigm	Cat# 3167011B; RRID: AB_2810974
Anti-human CD326(EpCAM)	Fluidigm	Cat# 3141006B; RRID: AB_2687653
Anti-human CD4	Fluidigm	Cat# 3176010B; RRID: AB_2810247
Anti-human CD45	Fluidigm	Cat# 3089003B; RRID: AB_2661851
Anti-human CD8a	Fluidigm	Cat# 3146001B; RRID: AB_2687641
Anti-human CD90	Fluidigm	Cat# 3159007B
Anti-human CDKN2A/p16INK4a	Abcam	Cat# ab186932
Anti-human IL-6	Fluidigm	Cat# 3147002B
Anti-human PDGFRa(CD140A)	Fluidigm	Cat# 3160007A
APC anti-human CD45	TOMBO	Cat# 20-0459-T025
Brilliant violet 510 anti-human CD326(EpCAM)	BioLegend	Cat# 324236; RRID: AB_2632935
Goat anti-rabbit IgG-HRP	Cell Signaling Technology	Cat# 7074; RRID: AB_2099233
Mouse monoclonal to a-Tubulin	Abcam	Cat# ab7291; RRID: AB_2241126
Mouse monoclonal to gH2AX	Millipore	Cat# 05-636; RRID: AB_309864
Mouse monoclonal to H3K27me3	Abcam	Cat# ab6002; RRID: AB_305237
Mouse monoclonal to p15 INK4B	Santa Cruz	Cat# sc271791, RRID: AB_10709436
PE anti-human CD90	BioLegend	Cat# 328110; RRID: AB_893433
PE-Cy7 anti-human CD140a(PDGFRa)	BioLegend	Cat# 323507; RRID: AB_2565596
Rabbit pSTQ	Cell Signaling Technology	Cat# 2851; RRID: AB_330318
Rabbit Ezh2	Cell Signaling Technology	Cat# 5246; RRID: AB_10694683
Rabbit Lamin B1	Abcam	Cat# ab16048; RRID: AB_10107828
Rabbit monoclonal to GAPDH	Cell Signaling Technology	Cat# 5174; RRID: AB_10622025
Rabbit monoclonal to Ki67	Spring Bioscience	Cat# M3062; RRID: AB_11219741
Rabbit monoclonal to NFkB1 p65	Cell Signaling Technology	Cat# 8242; RRID: AB_10859369
Rabbit monoclonal to p16 INK4A	Abcam	Cat# ab108349; RRID: AB_10858268
Rabbit monoclonal to p38	Cell Signaling Technology	Cat# 8690; RRID: AB_10999090
Rabbit monoclonal to p-Erk1/2	Cell Signaling Technology	Cat# 4370; RRID: AB_2315112
Rabbit monoclonal to p-Stat3	Cell Signaling Technology	Cat# 9145; RRID: AB_2491009
Rabbit monoclonal to Stat3	Cell Signaling Technology	Cat# 4904; RRID: AB_331269
Rabbit polyclonal to Akt	Cell Signaling Technology	Cat# 9272; RRID: AB_329827
Rabbit polyclonal to anti-β-Actin	Cell Signaling Technology	Cat# 4967; RRID: AB_330288
Rabbit polyclonal to Bcl-2	Cell Signaling Technology	Cat# 2872; RRID: AB_10693462
Rabbit polyclonal to Erk1/2	Cell Signaling Technology	Cat# 9102; RRID: AB_330744
Rabbit polyclonal to H3K27me3	Millipore	Cat# 07-449; RRID: AB_310624
Rabbit polyclonal to Histone3	Abcam	Cat# ab1791; RRID: AB_302613
Rabbit polyclonal to p-Akt	Cell Signaling Technology	Cat# 9271; RRID: AB_329825
Rabbit polyclonal to p-p38	Cell Signaling Technology	Cat# 9125; RRID: AB_2140644

(*Continued on next page*)

Continued

REAGENT or RESOURCE	SOURCE	IDENTIFIER
Bacterial and virus strains		
ECOSTM Competent *E. coli* DH5 α	NIPPON GENE	Cat# 310-06236
pLenti-C-Myc-DDK-IRES-Puro Tagged Cloning Vector	OriGene	Cat# PS100069
Zero Blunt TOPO PCR Cloning Kit, without competent cells	Invitrogen	Cat# 450245
Biological samples		
Gastric cancer tissue from patients	This paper	N/A
Serum from patients	This paper	N/A
Chemicals, peptides, and recombinant proteins		
DNase I, Amplification Grade	Thermo Fisher Scientific	Cat# 18068015
ERCC RNA Spike-In Mix	Thermo Fisher Scientific	Cat# 4456740
Halt Protease and Phosphatase Inhibitor Cocktail (100X)	Thermo Fisher Scientific	Cat# 78442
Human TruStain FcX	BioLegend	Cat# 422301
Incucyte® NucLight Rapid Red Reagent for nuclear labeling	Essen BioScience	Cat# 4717
InSolution STAT3 Inhibitor III, WP1066	Millipore	Cat# 573129
Klenow Fragment (3′-5′ exo-)	New England Biolabs	Cat# M0212
Lipofectamine® RNAiMAX Transfection Reagent	Thermo Fisher Scientific	Cat# 13778-150
LipofectamineTM 3000	Thermo Fisher Scientific	Cat# L3000015
Maxpar® Fix I Buffer	Fluidigm	Cat# 201065
Maxpar® Perm-S Buffer	Fluidigm	Cat# 201066
Maxpar® Water	Fluidigm	Cat# 201069
MluI-HF	New England Biolabs	Cat# R3198S
NEBuffer 2	New England Biolabs	Cat# B7002
NP40 Cell Lysis Buffer	Thermo Fisher Scientific	Cat# FNN0021
Oligo(dT)12-18 Primer	Thermo Fisher Scientific	Cat# 18418012
Oligo(dT)18 Primer	Thermo Fisher Scientific	Cat# SO131
Random Primers	Thermo Fisher Scientific	Cat# 48190011
RealTime ready Cell Lysis Buffer	Roche	Cat# 7248431001
RIPA buffer	Thermo Fisher Scientific	Cat# 89901
RNaseOUT Recombinant Ribonuclease Inhibitor	Thermo Fisher Scientific	Cat# 10777019
RNasin Plus RNase Inhibitor	Promega	Cat# PAN2615
RPMI-1640	FUJIFILM Wako Pure Chemical Corporation	Cat# 189-02145
SuperScript III Reverse Transcriptase	Thermo Fisher Scientific	Cat# 18080093
T4 Gene 32 Protein	New England Biolabs	Cat# M0300
VivoGlo Luciferin, *In Vivo* Grade	Promega	Cat# P1043
Critical commercial assays		
Absolute Human Telomere Length Quantification qPCR Assay Kit	ScienCell	Cat# 8918
DCFDA/H2DCFDA-Cellular ROS Assay Kit	Abcam	Cat# ab113851
Lentiviral High Titer Packaging Mix	TaKaRa	Cat# 6194
miRneasy Mini Kit	QIAGEN	Cat# 74106
Mouse C-Reactive Protein/CRP Quantikine ELISA Kit	R&D Systems	Cat# MCRP00
PrimeScript RT reagent Kit	TaKaRa	Cat# RR037A

(*Continued on next page*)

Continued

REAGENT or RESOURCE	SOURCE	IDENTIFIER
QIAamp DNA Mini Kit	QIAGEN	Cat# 51306
QIAquick PCR Purification Kit (250)	QIAGEN	Cat# 28106
Senescence Detection Kit	BioVision	Cat# K320
ThruPLEX DNA-seq Kit	TaKaRa	Cat# R400674
TUNEL Assay Kit - BrdU-Red	Abcam	Cat# ab66110
Zombie Green Fixable Viability Kit	BioLegend	Cat# 423111
Deposited data		
RNA sequencing data	This paper	DRA008307
ChIP sequencing data	This paper	DRA011193
Experimental models: cell lines		
Human: OCUM2MD3	N/A	RRID:CVCL_8385
Human: NUGC3	Japanese Collection of Research Bioresources Cell Bank	Cat# JCRB0822; RRID:CVCL_1612
Lenti-X 293T cell line	TaKaRa	Cat# Z2180N
Experimental models: organisms/strains		
Mouse: BALB/cAJcl-nu/nu	CLEA Japan, Inc	N/A
Oligonucleotides		
Primer sequences	see Table S2.	N/A
Recombinant DNA		
Silencer Select Negative Control No. 1 siRNA	Thermo Fisher Scientific	Cat# 4390843
siRNA targeting RELA	Thermo Fisher Scientific	Assay ID: s11914 Cat# 4427038
siRNA targeting STAT3	Thermo Fisher Scientific	Assay ID: s744 Cat#4427038
Recombinant Human IL-6	PeproTech	Cat# 200-06
Recombinant Human IL-1α	Bay Bioscience	Cat# 8019
Recombinant Human IL-1b	Bay Bioscience	Cat# 8018
Recombinant Human TNF-α	Bay Bioscience	Cat# 8329
Software and algorithms		
2100 Bioanalyzer	Agilent	https://www.chem-agilent.com/contents.php?id=51
Bowtie2	Langmead and Salzberg, 2012	http://bowtie-bio.sourceforge.net/bowtie2/index.shtml
BZ-X Analyzer	Keyence	https://www.keyence.co.jp/
FastQC	Babraham Bioinformatics	http://www.bioinformatics.babraham.ac.uk/projects/fastqc/
FlowJo 3.3 software	BD Biosciences	https://www.bdbiosciences.com/jp/instruments/software/flowjo/index.jsp
FlowSOM	(Van Gassen et al., 2015)	http://bioconductor.org/packages/release/bioc/html/FlowSOM.html
ImageJ	NIH	https://imagej.nih.gov/ij/
Incucyte® S3 Live-Cell Analysis System	Essen BioScience	https://www.essenbioscience.com/ja/products/incucyte/incucyte-s3/
JMP version 9	SAS Institute	https://www.sas.com/ja_jp/home.html
LUNA-II Automated Cell Counter	Logos Biosystems	Cat# T13001
NextSeq 500	Illumina	https://www.biocompare.com/23967-Next-Generation-Sequencers/11182085-NextSeq-500-System/

RESOURCE AVAILABILITY

Lead contact

Further information and requests for resources and reagents should be directed to and will be fulfilled by the Lead Contact, Takatsugu Ishimoto (taka1516@kumamoto-u.ac.jp).

Materials availability

All materials will be made available upon reasonable request.

Data and code availability

All data are available within the article. Sequencing data that support the funding of this study have been deposited in DDBJ under the accession numbers listed below. RNA sequencing: DRA008307. ChIP sequencing: DRA011193.

EXPERIMENTAL MODEL AND SUBJECT DETAILS

Patients and tissue samples

Laboratory data were obtained from patients (ages 56-78 years of either sex) who underwent a gastrectomy at the Department of Gastroenterological Surgery, Kumamoto University Hospital (Kumamoto, Japan). Primary CAFs and NFs were isolated from patients (ages 52-74 years of either sex) with GC who underwent gastrectomy without preoperative treatment at Kumamoto University, Saiseikai Kumamoto Hospital after informed consent was obtained from each patient. Serum samples were obtained from patients at the Department of Gastroenterological Surgery, Kumamoto University Hospital (Kumamoto, Japan). The study was approved by the Medical Ethics Committee of Kumamoto University (Approval Number: 1277) and Saiseikai Kumamoto Hospital (Approval Number: 362).

Cell lines and cell culture

The human GC cell line NUGC3 was obtained from the Japanese Collection of Research Bioresources Cell Bank and the RIKEN BioResource Center Cell Bank. OCUM-2MD3 cells were derived from a peritoneal metastatic nodule after orthotopic implantation of OCUM-2M cells, which were derived from a 49-year-old female with scirrhous gastric cancer in 1992. Human gastric fibroblast cell lines were derived from the surgically excised gastric tissue of 100 patients with GC. CAFs were established from the surgically excised gastric wall tumor, and NFs were from the non-tumor gastric wall tissue. These cells were cultured in RPMI 1640 containing 10% FBS (normal medium) and incubated at 37°C with 5% CO_2.

Animals

Eight- to ten-week-old male BALB/c nude mice (Clea Japan, Shizuoka, Japan) were housed in a room under stable temperature and humidity on a 12 hour-light and dark cycle. Both water and food were supplied adlibitum. All animal procedures and studies were conducted in accordance with the Institutional Animal Care and Use Committee (IACUC) at Kumamoto University (Approval Number: F29-189).

METHOD DETAILS

Conditioned media experiments

For conditioned media experiments, CAFs were treated for 24 hours with three inflammatory cytokines (3CKs), IL1α, IL1β, and TNFα, at 10 ng/ml each (Bay Bioscience, Japan) in RPMI 1640 containing 10% FBS. Media were collected, centrifuged to remove debris, and filtered with a Millex Sterile Filter Unit, 0.22 μm (Millipore). CAF-conditioned medium (CM) was collected from CAFs, and S-CAF-CM was collected from S-CAFs induced by 3CKs for 24 hours and then cultured in normal medium.

Drugs and recombinant proteins used for *in vitro* experiments

Recombinant human IL-6 (PeproTech) and the JAK/STAT3 inhibitor WP1066 (Millipore) were purchased. Cells were treated with 10 ng/ml recombinant human IL-6 or 5 μM WP1066 for each *in vitro* experiment.

Animal experiments

Eight- to ten-week-old male BALB/c nude mice (Clea Japan, Shizuoka, Japan) were housed in Kumamoto University (Approval Number: F29-189). OCUM-2MD3 cells (5.0×10^6) were implanted through intraperitoneal injection. Tumor weight and body weight were evaluated in these mice. Three groups of mice were assessed for tumor development: 1) tumor-bearing mice treated with normal medium (NM) (n = 8), 2) tumor-bearing mice treated with CAF-CM, and 3) tumor-bearing mice treated with S-CAF-CM. The mice were treated with each CM (200 μl/day) via an intraperitoneal injection every day for 30 days. The mice were sacrificed 30 days after tumor cell inoculation. For the JAK/STAT3 inhibitor (WP1066) study, two groups of tumor-bearing mice were anaesthetized by isoflurane inhalation, and tumor growth was assessed using an *in vivo* imaging system (Caliper IVIS Kinetic *In Vivo* Optical Imaging

System) after a luciferin injection (200 mg/kg). Two groups of mice treated with daily S-CAF-CM were assessed for tumor development and were either treated with vehicle (DMSO, control) or 20 mg/kg WP1066 a total of 8 times for 3 weeks. Control mice received volumes of DMSO equivalent to the volumes of WP1066 used to treat the mice. For the recombinant IL-6 study, tumor-bearing mice were injected with 200 ng/mouse of recombinant human IL-6 or 200 μL of PBS a total of 12 times for 30 days.

DNA and RNA extraction

Genomic DNA and total RNA were extracted from cultured cells using a QIAamp DNA Mini Kit (QIAGEN, Hilden, Germany) and a miRNeasy Mini Kit (QIAGEN), respectively, according to the manufacturer's instructions.

Quantitative reverse transcription-PCR

Complementary DNA (cDNA) was reverse transcribed from total RNA using SuperScript III, RNaseOUT, Recombinant Ribonuclease Inhibitor, Random Primers and Oligo(dT)12–18 Primer (Thermo Fisher Scientific). Quantitative reverse transcriptase (qRT)-PCR was performed using the TaqMan Probe method. All primers and probe sets were designed by the Universal Probe Library Assay Design Center. All primers were synthesized by GeneNet, and all probes were purchased from Roche Diagnostics. The qRT-PCR assay was performed as previously described (Ishimoto et al., 2017). Primer and probe sequences for each Custom TaqMan Gene Expression Assay are listed in Table S2.

RNA sequencing

RNA sequencing was performed by Liaison Laboratory Research Promotion Center (LILA) (Kumamoto University) using the method described below. A 2100 Bioanalyzer (Agilent) was used to detect the concentration and purity of the total RNA. All samples with an RNA integrity number (RIN) > 8.0 were used for sequencing. A NextSeq 500 (Illumina) instrument was used for the analysis, and the data were converted to Fastq files. The quality control of the data was performed with FastQC. Then, the filtered reads were mapped to the UCSC hg19 reference genome using HISAT2 (v2.1.0). The fragments per kilobase of exon per million mapped reads (FPKM) values were calculated using Cufflinks (v2.2.1) software. Significant genes were extracted using Cuffdiff ($p < 0.05$).

Chromatin IP sequencing

ChIP-seq was performed as described previously (Kubota et al., 2019). CAFs were fixed with 0.5% paraformaldehyde at 37°C for 5 min and then lysed. Cells were sonicated 15 times at a 50% amplitude for 10 s each. Samples were incubated with anti-H3K27me3 antibody-conjugated (Abcam) or anti-mouse IgG-conjugated Dynabeads at 4°C overnight. Input and immunoprecipitates were incubated at 65°C for 4 h to reverse cross-links, and DNA was purified using the QIAquick PCR Purification Kit (250) (QIAGEN, #28106). ChIP-seq libraries were generated using the ThruPLEX DNA-seq kit (Takara). Bowtie2 (version 2.2.6; default parameters) was used to map the reads to the reference genome (UCSC/hg19) (Langmead and Salzberg, 2012). Bedtools and HOMER (version 4.9) were used to count reads and assess reads coverage. ChIP-sequencing data were deposited in the DDBJ database under the accession number DRA011193.

Expression vectors

The human EZH2 cDNA was amplified with a forward primer (5′- GAATAATCATGGGCCAGACTGGGAAGAAATCTG-3′) and a reverse primer (5′- ATGTCAAGGGATTTCCATTTCTCTTTCGATGC-3′) using cDNA isolated from CMK cells as a template, and the product was ligated into pCR-Blunt II-TOPO (Invitrogen). The full sequence of the EZH2 cDNA was validated by Sanger sequencing. The ORF of *EZH2* was PCR amplified with a forward primer with an AsiSI site (5′-GAGGCGATCGCCATGGGCCAGACTGGGAAG-3′) and a reverse primer with an MluI site (5′-GCGACGCGTTCAAGGGATTTCCATTTCTCTTTCGATG-3′) to append the cloning sites. The ORF was cloned into the destination vector pLenti-C-Myc-DDK-IRES-Puro Tagged Cloning Vector (Origene, #PS100069) using AsiSI (New England Biolabs) and MluI (New England Biolabs). The PCR product was separated by agarose gel electrophoresis and purified with the QIAquick PCR Purification Kit (250) (QIAGEN, #28106). The PCR product and pLenti-C-Myc-DDK-IRES-Puro Tagged Cloning Vector were digested with AsiSI and MluI, purified, and ligated using a ligation mix. Transformation was performed in competent *E. coli* DH5 α (NIPPON GENE, #310-06236) according to the ECOS™ 1 min/6 min protocol from ECOS™. Lentivirus particles were produced using the Lentiviral High Titer Packaging Mix (TaKaRa: 6194) according to the manufacturer's protocol. Briefly, the destination vectors and Lentiviral High Titer Packaging Mix were transfected into cells from the Lenti-X 293T Cell Line (TaKaRa: Z2180N) using Lipofectamine 3000 (Thermo Fisher Scientific). After a 48-hour incubation, the media containing lentivirus particles were collected and passed through a 0.45-mm filter. To establish EZH2-overexpressing CAFs, CAFs were cultured in complete medium containing virus particles with 4 μg/ml polybrene for 24 hours.

Western blot analysis

Cultured cells were lysed with RIPA buffer containing a protease and phosphatase inhibitor cocktail (Thermo Fisher Scientific). The lysate was sonicated, the debris were removed by centrifugation, and the supernatant was collected as a whole-cell lysate. Protein samples were subjected to SDS-PAGE, transferred to PVDF membranes, and blotted with the primary antibodies in Can Get Signal Solution 1 (Toyobo) at 4°C overnight. The signals were detected after an incubation with rabbit or mouse secondary antibodies in Can Get Signal Solution 2 at room temperature for 1 hour using an ECL Detection System (GE Healthcare, Little Chalfont,

Buckinghamshire, UK). The antibodies against the corresponding molecules are listed in Table S1. The quantification of the band signals was performed with ImageJ software (NIH, USA)

ELISA

Serum levels of CRP in tumor-bearing mice were measured using an ELISA (R&D Systems). The assay procedure was performed according to the manufacturer's protocol.

Immunofluorescence and immunohistochemical staining

All tissue slices (4-mm thick) were cut from formalin-fixed, paraffin-embedded tissues and mounted on slide glass. The sections were prepared for heat-induced antigen retrieval via autoclaving in 1X Antigen Retrieval Solution. All cells were cultured on a 35-mm glass-bottom dish (Matsunami, Japan). The dishes were fixed with 4% paraformaldehyde in phosphate buffer and permeabilized with 0.5% Triton X-100 in PBS. Subsequently, each slide or dish was washed with PBS and stained with the primary antibody overnight at 4°C. For immunofluorescence (IF) staining, the Alexa Fluor 488- or 594-conjugated secondary antibodies were incubated with the sections for 1 hour at room temperature. For immunohistochemistry (IHC), the HRP-conjugated anti-rabbit secondary antibody (Dako, Japan) was incubated with the sections. The slides were visualized using a BZ-X710 microscope (KEYENCE). The antibodies used are listed in Table S1. Apoptosis was evaluated by performing a TUNEL assay using an *In Situ* BrdU-Red DNA Fragmentation (TUNEL) Assay Kit (Abcam, ab66110).

Cell proliferation assay

CAFs were seeded in 96-well plates at a density of 1.0×10^3 cells/well and incubated at 37°C with 5% CO_2. At 24 hours after seeding, the CAFs were exposed to pro-inflammatory cytokines (IL1α, IL1β, and TNFα). OCUM-2MD3 cells were seeded into 6-well plates at a density of 2.0×10^5 cells/well and incubated at 37°C with 5% CO_2. At 24 hours after seeding, cells were exposed to either S-CAF-CM or CAF-CM for 48 hours. Cell proliferation was then measured with a Luna cell counting plate or using an IncuCyte S3 Livecell Analysis system (Essen BioScience). For the analysis with the IncuCyte system, CAFs were seeded into 96-well plates and stained with Nuc-Light Rapid Red (Essen BioScience). The plate was inserted into the IncuCyte instrument for real-time imaging, with four fields imaged per well every 24 hours over 10 days. Data were analyzed using the IncuCyte software, which quantified the percentage of red confluence values. All groups were tested in triplicate, and the data are presented as the means ± standard errors of the means (SEM).

Flow cytometry

The cell concentration was adjusted to 1×10^6 cells/ml in PBS containing 2% FBS. The cell suspensions were incubated with antibodies (Table S1) for 30 minutes on ice, washed with PBS containing 2% FBS and centrifuged twice, and the cell pellet was suspended in PBS. Flow cytometry was performed with a FACSVerse instrument (BD Biosciences). The flow cytometry data were analyzed using FlowJo 3.3 software (Tree Star).

Small interfering RNA (siRNA) transfection

RELA (NFκB p65) and STAT3 expression were downregulated by transfecting cells with predesigned Silencer Select siRNAs directed against RELA (s11914, Cat# 4427038, Thermo Fisher Scientific) or STAT3 (s744, Cat# 4427038, Thermo Fisher Scientific), and a non-targeting siRNA (#4390843, Thermo Fisher Scientific) was used as the negative control. CAFs were transfected with annealed siRNAs for 24-48 hours using Lipofectamine RNAiMAX (#13778-150, Thermo Fisher Scientific).

ROS assay

ROS levels were assayed using the 2′,7'-dichlorofluorescin diacetate (DCFDA) cellular ROS assay kit (ab113851, Abcam) according to the manufacturers' protocol. Cells were transfected with annealed siRELA (siNFκB p65) for 24 hours, treated with 3CKs for 24 hours, and then cultured with normal medium for 2 days.

Cells were stained with buffer containing 25 μM DCFDA for 30 minutes at 37°C. After staining, cells were analyzed using flow cytometry.

Flow cytometry and cell sorting from ascites

Ascites was obtained from patients who underwent cell-free and concentrated ascites reinfusion therapy (CART) at the Kanamecho Hospital (Tokyo, Japan). The sample was collected by centrifugation, and red blood cells were lysed using ACK Lysis Buffer. The cells were adjusted to a concentration of 1×10^7 cells/ml in PBS with 2% FBS. Cell suspensions were incubated with antibodies for 30 min at 4°C. Cells were stained with a PE-conjugated anti-CD90 (Thy1) antibody (BioLegend, #328110), PE/Cy7-conjugated anti-CD140a (PDGFRα) antibody (BioLegend, #323507), BV510-conjugated anti-CD326 (EpCAM) antibody (BioLegend, # 324236), and APC-conjugated anti-CD45 (HI30) antibody (TOMBO, #20-0459-T025). Dead cells were removed with Zombie Green Fixable Viability Kit (BioLegend, # 423111). The cells were sorted on the FACSAriaII (BD Biosciences) to obtain CD90+/PDGFα, EpCAM+ and CD45+ cell populations.

RT-RamDa

Cells sorted by FACS were lysed in 10 μL of cell lysis buffer containing 40 U of RNasin Plus (Promega), Roche Cell Lysis Buffer (Roche), 10% NP40 (Thermo Fisher), and RNase-free water (TaKaRa). The lysate was centrifuged and mixed using a ThermoMixer C (Eppendorf) at 2000 rpm for 1 min at 4°C. Template RNA was diluted in 10 μL of lysis buffer, denatured for 1.5 min at 70°C, and stored on ice. The reaction buffer for RT was modified using the PrimeScript RT Reagent Kit (TaKaRa). A genomic DNA digestion solution containing 5 × RT buffer (TaKaRa), 1 U of DNase I, Amplification Grade (Thermo), and ERCC RNA Spike-In Mix 1 (Thermo) was added to the sample plate and incubated in a thermal cycler for 5 min at 30°C. A mixture containing 5 × RT buffer, 20 × Enzyme Mix (TaKaRa), 1 mg/ml T4 gene 32 protein (NBE), 30 μM oligo(dT)18 (Thermo Fisher), and 100 μM 1st NSR primer for human (Sigma) was added to the template RNA. The mixture was agitated and incubated in a thermal cycler at 25°C for 10 min, 30°C for 10 min, 37°C for 30 min, 50°C for 5 min, and 94°C for 5 min. A second-strand synthesis solution containing 10 × NBE buffer 2 (NBE), 25 mM dNTPs (TaKaRa), 100 μM 2nd NSR primer for human (Sigma), and Klenow fragment (NBE) was added to the RT product. The mixture was agitated and incubated in a thermal cycler at 16°C for 60 min and at 70°C for 10 min. The product was diluted in nuclease-free water and used for the qPCR analysis.

Mass cytometry

Cells from patients' ascites were collected as described above. A total of 3.0×10^6 cells were labeled with Cell-ID Cisplatin (Fluidigm) to determine whether the cells were alive or dead. Human TruStain FcX (BioLegend) was added to each cell pellet. For staining cell surface antigens, cells were resuspended in cell staining cocktail (Table S3). Cells were fixed using FixI buffer (Fluidigm) and washed with Maxpar Perm-S Buffer (Fluidigm). An antibody cocktail (Table S3) was added to stain cytoplasmic antigens. Methanol was added to each tube for fixation and permeabilization. An antibody cocktail (Table S3) was added to stain nuclear antigens. Cells were labeled for single-cell discrimination with Cell-ID Intercalator-Ir (Fluidigm). Cells were washed with Maxpar Water (Fluidigm) and then diluted in water containing 10% EQ Calibration Beads and run on the Helios CyTOF system for sample acquisition. Mass cytometry data were analyzed using Cytobank software. The viSNE analysis, an application of stochastic neighbor embedding (SNE), was performed using Cytobank applications employing the Barnes–Hut implementation of t-SNE. Cell populations were identified utilizing a FlowSOM (Van Gassen et al., 2015) and applying the FlowSOM clustering algorithm on Cytobank. Heatmaps of relative marker expression were generated using Morpheus from the Broad Institute (https://software.broadinstitute.org/morpheus).

Telomere length quantification

A qPCR assay for quantifying the telomere length was performed using the Absolute Human Telomere Length Quantification qPCR Assay Kit (ScienCell) according to the manufacturer's instructions. The average telomere lengths of samples were directly compared with the reference human genomic DNA sample primer set that recognized and amplified telomere sequences.

SA-β-gal assay

The SA-β-gal assay was performed using a Senescence Detection Kit (BioVision). Cells were fixed with fixative solution and stained with a staining solution mix (Staining Solution, Staining Supplement, 20 mg/ml X-gal in DMSO) overnight at 37°C. Cells were then washed twice with PBS, and the percentage of stained cells was determined.

QUANTIFICATION AND STATISTICAL ANALYSIS

All experiments were performed in triplicate, and the data shown are representative of consistently observed results. Data are presented as the mean ± standard deviation (SD). The Mann-Whitney U test was used to compare continuous variables between 2 groups. Data were analyzed using JMP (version 9, SAS Institute, Japan). p value < 0.05 were considered statistically significant. All p values and n are reported in the figure legends.

Cell Reports, Volume *34*

Supplemental information

Inflammation-driven senescence-associated secretory phenotype in cancer-associated fibroblasts enhances peritoneal dissemination

Tadahito Yasuda, Mayu Koiwa, Atsuko Yonemura, Keisuke Miyake, Ryusho Kariya, Sho Kubota, Takako Yokomizo-Nakano, Noriko Yasuda-Yoshihara, Tomoyuki Uchihara, Rumi Itoyama, Luke Bu, Lingfeng Fu, Kota Arima, Daisuke Izumi, Shiro Iwagami, Kojiro Eto, Masaaki Iwatsuki, Yoshifumi Baba, Naoya Yoshida, Hiroto Ohguchi, Seiji Okada, Keisuke Matsusaki, Goro Sashida, Akiko Takahashi, Patrick Tan, Hideo Baba, and Takatsugu Ishimoto

Supplemental Information

Inflammation-driven Senescence-associated Secretory Phenotype in Gastric Cancer-associated Fibroblasts Enhances Peritoneal Dissemination

Tadahito Yasuda, Mayu Koiwa, Atsuko Yonemura, Keisuke Miyake, Ryusho Kariya, Sho Kubota, Takako Yokomizo-Nakano, Noriko Yasuda-Yoshihara, Tomoyuki Uchihara, Rumi Itoyama, Luke Bu, Lingfeng Fu, Kota Arima, Daisuke Izumi, Shiro Iwagami, Kojiro Eto, Masaaki Iwatsuki, Yoshifumi Baba, Naoya Yoshida, Hiroto Ohguchi, Seiji Okada, Keisuke Matsusaki, Goro Sashida, Akiko Takahashi, Patrick Tan, Hideo Baba and Takatsugu Ishimoto

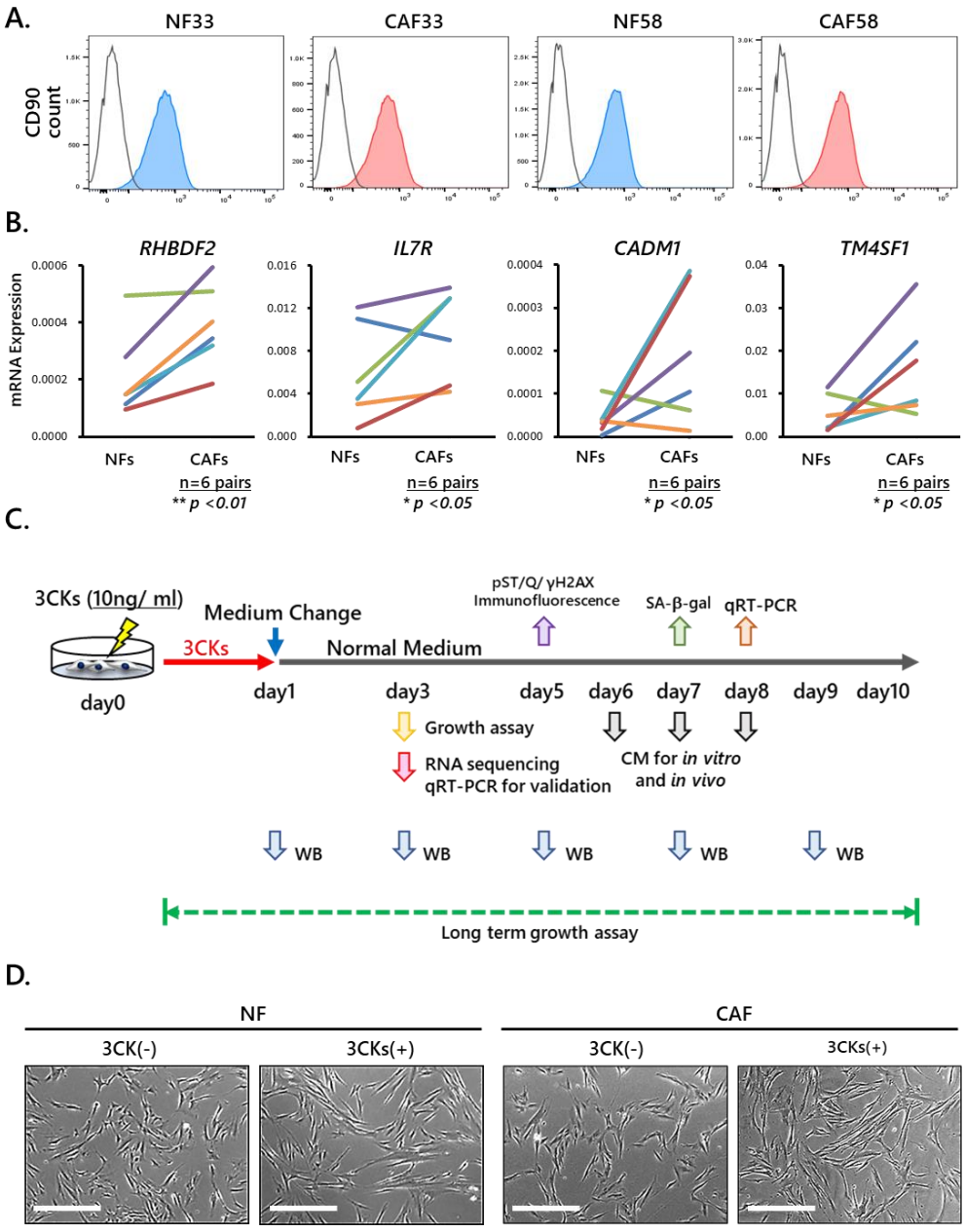

Supplementary Figure 1. Characterization of cultured fibroblasts and experimental procedure used in this study. Related to Figure 1, 2, 3, 5 and 6.

(A) Flow cytometry analysis of CD90 expression in NFs and CAFs. (B) RT-qPCR analysis of the *RHBDF2*, *IL7R*, *CADM1*, and *TM4SF1* mRNAs in NFs and CAFs. Data were normalized to the level of the *β-actin* mRNA (**p< 0.01; *p< 0.05, n=6 pairs). (C) Timeline of the experimental procedure for sample collection. (D) NFs and CAFs treated with 3CKs had larger and more spindles than the control. Scale bars, 500 μm.

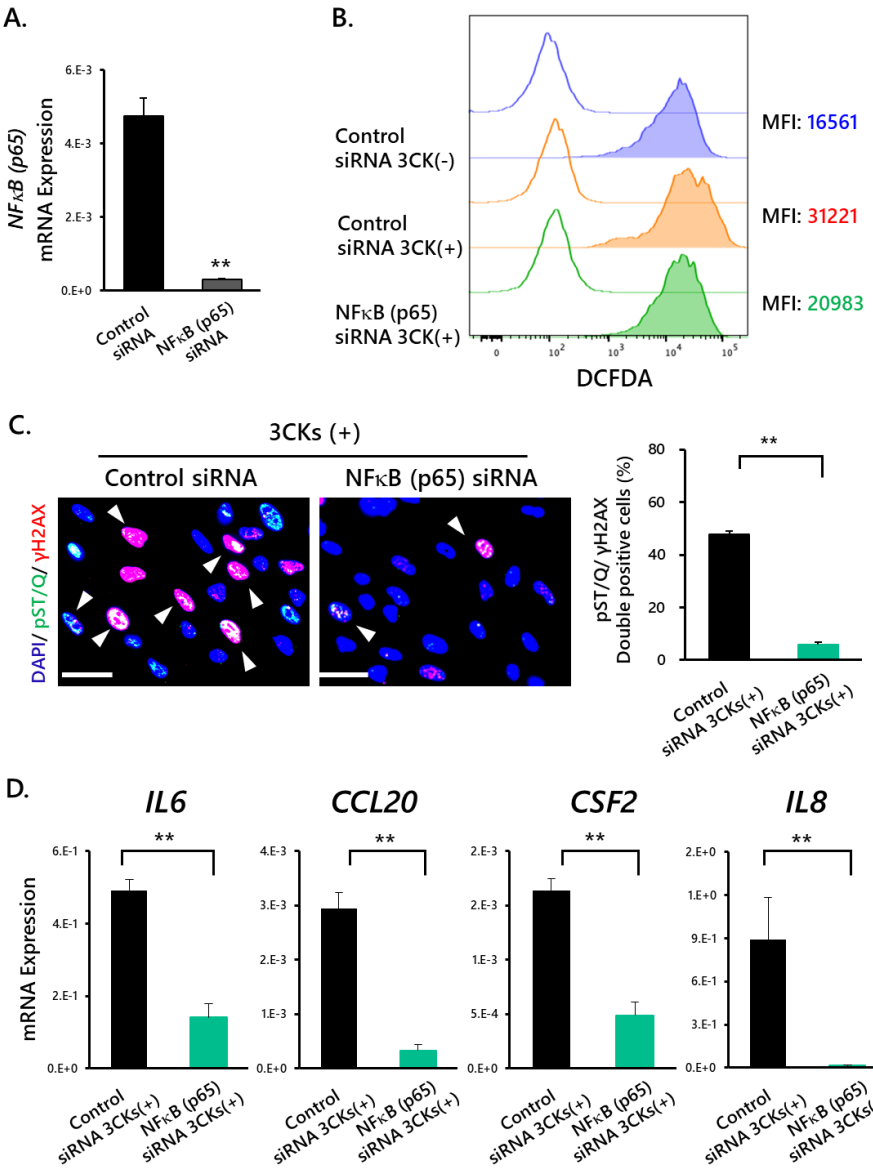

Supplementary Figure 2. The involvement of the NFκB transcription factor in regulating the senescent status of CAFs treated with 3CKs. Related to Figure 1.

(A) RT-qPCR analysis of the NFkB (p65) mRNA in CAFs transfected with an NFkB (p65) siRNA compared to CAFs transfected with the control siRNA (**p < 0.01, n=3). (B) Histograms represent ROS levels in CAFs transfected with the NFkB siRNAs and treated with 3CKs relative to CAFs transfected with the control siRNA. (C) Immunofluorescence staining for markers of DNA damage (γ-H2AX and pST/Q substrate) together with nuclear staining with DAPI in CAFs transfected with the control siRNA or NFkB (p65) siRNA 5 days after the 3CK treatment. Scale bars, 50 μm. The graph shows the percentage of nuclei with double-positive staining for γ-H2AX and pST/Q (**p < 0.01, n=3). (D) RT-qPCR analysis of SASP factors in CAFs transfected with the control siRNA or NFkB (p65) siRNA 3 days after the 3CK treatment (**p < 0.01, n=3).

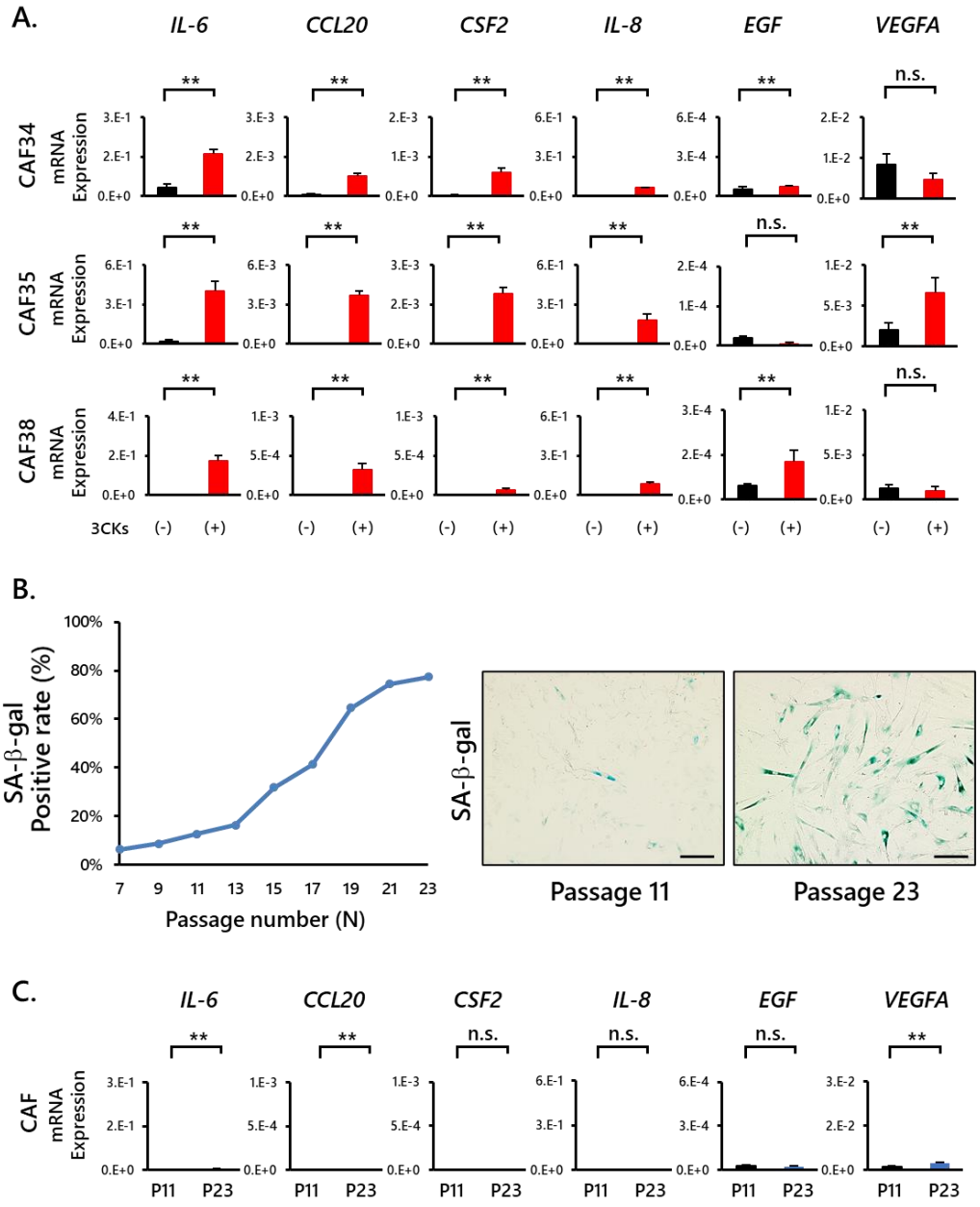

Supplementary Figure 3. The expression of SASP factors induced by 3CKs and by long-term passaging. Related to Figure 2.

(A) RT-qPCR analysis of SASP factors 7 days after the 3CK treatment (**p < 0.01; n.s., not significant, n=3). (B) The graphs show the transition of the percentage of SA-β-gal-positive cells for up to twenty-three passages. At least one hundred cells were counted. Representative images of each CAF line after early and long passage numbers. Scale bars, 500 μm. (C) RT-qPCR analysis of SASP factors in CAFs subjected to long-term passaging (**p < 0.01; n.s., not significant, n=3).

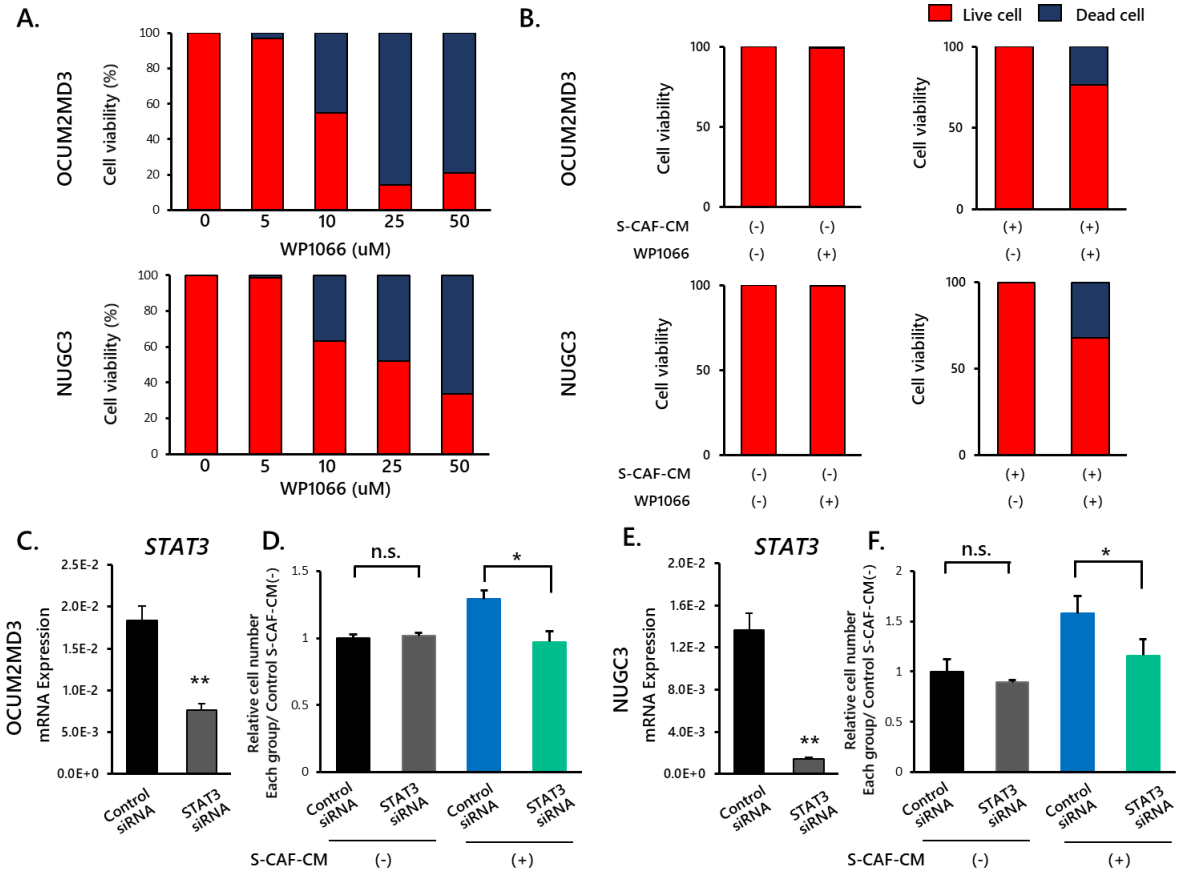

Supplementary Figure 4. SASP factors from S-CAFs enhance GC cell growth through JAK/STAT3 signaling. Related to Figure 3.

(A) Viability of OCUM-2MD3 cells and NUGC3 cells treated with various concentrations of WP1066 for 3 days. (B) Viability of WP1066-treated OCUM-2MD3 and NUGC3 cells incubated with or without S-CAF-CM. We collected S-CAF-CM from S-CAFs induced by 3CKs. (C) RT-qPCR analysis of the STAT3 mRNA in OCUM-2MD3 cells transfected with the STAT3 siRNA compared to OCUM-2MD3 cells transfected with the control siRNA (**p< 0.01, n=3). (D) Growth assays of OCUM-2MD3 cells treated with S-CAF-CM, vehicle (DMSO) or WP1066 for 3 days (*p< 0.05; n.s., not significant, n=3). (E) RT-qPCR analysis of the STAT3 mRNA in NUGC3 cells transfected with the STAT3 siRNA compared to NUGC3 cells transfected with the control siRNA (**p< 0.01, n=3). (F) Growth assays of NUGC3 cells treated with S-CAF-CM, vehicle (DMSO) or WP1066 for 3 days (*p< 0.05; n.s., not significant, n=3).

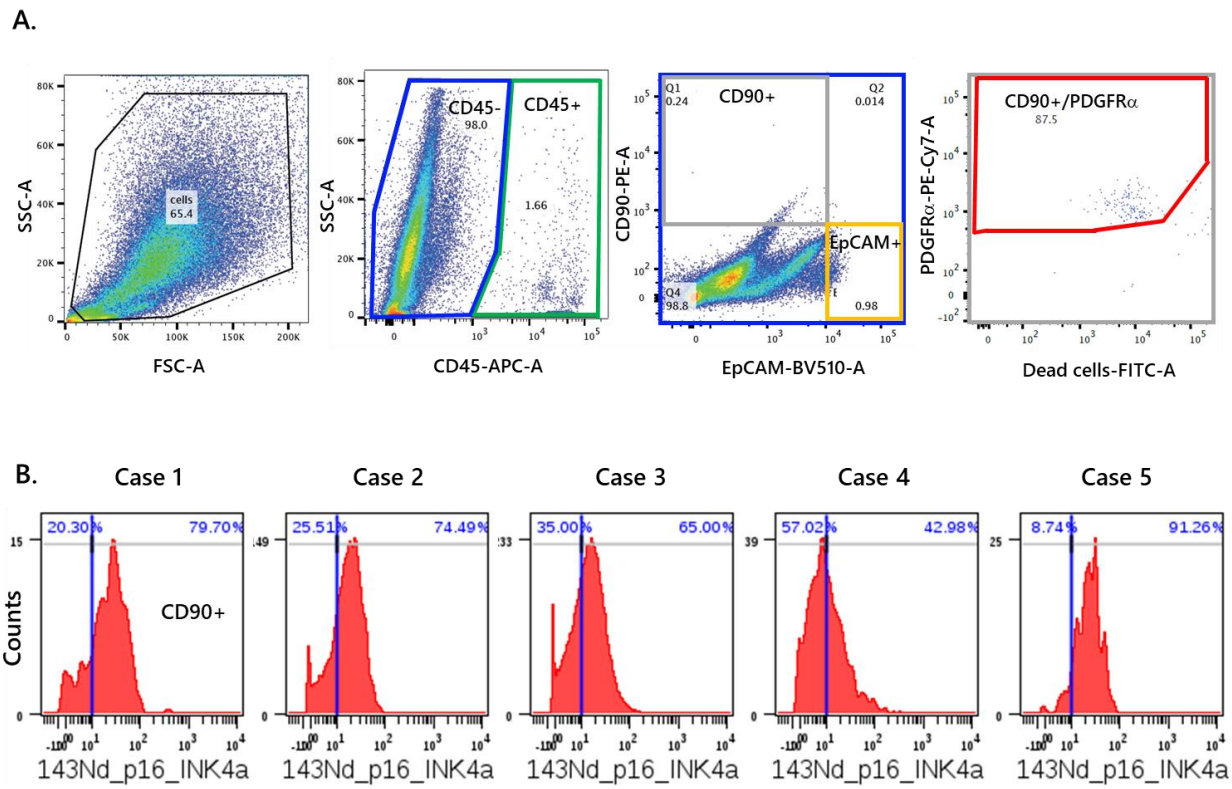

Supplementary Figure 5. Three labelled populations from ascites of patients with GC and the p16 expression level in CD90(+) fibroblasts. Related to Figure 4.

(A) Flow charts showing the gating strategy for sorting each labelled population (CD90/PDGFRα, EpCAM, and CD45) from ascites from patients with GC used for the analysis of SASP expression. (B) Histograms represent the expression of p16 levels in the CD90-labelled population.

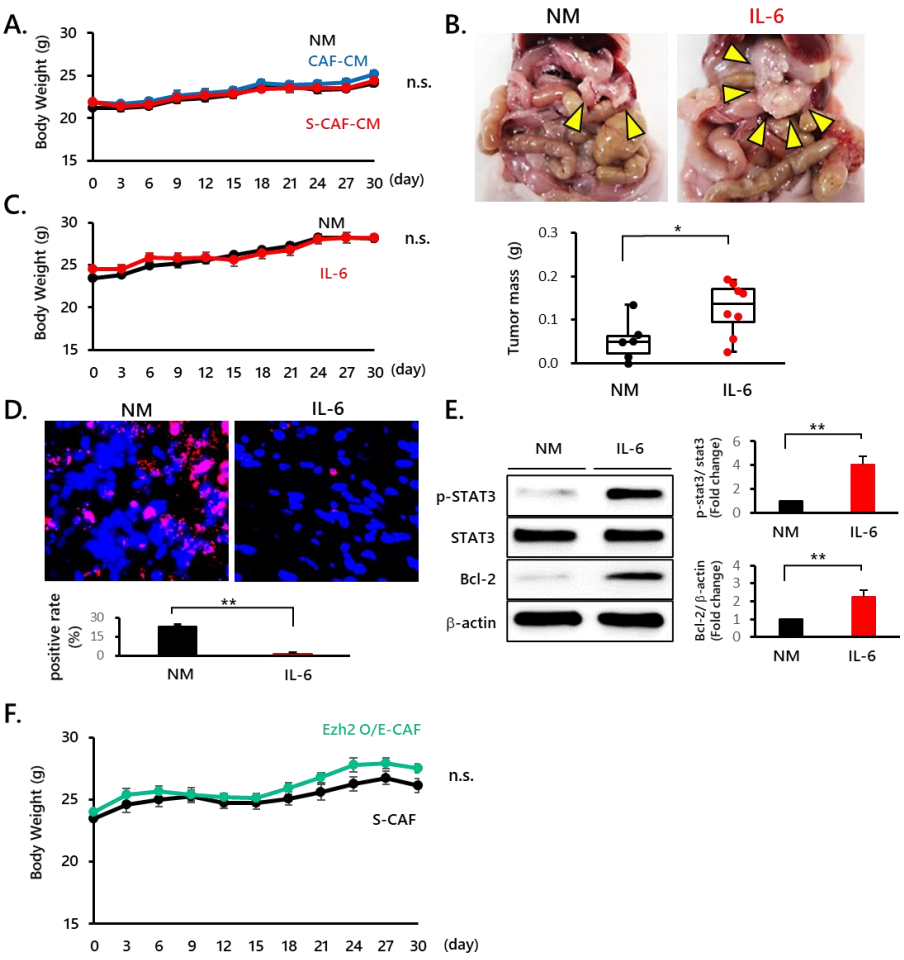

Supplementary Figure 6. IL-6 activates JAK/STAT3 signaling and promotes peritoneal tumor formation by inhibiting apoptosis without harm. Related to Figure 5.

(A) Body weight changes after daily intraperitoneal injections of CAF-CM or S-CAF-CM compared to animals injected with the normal medium. No significant difference in mouse body weight was observed among the three groups during treatment. (B) Representative images of OCUM-2MD3-bearing mice treated with vehicle (NM) or IL-6 (200 ng/mouse) a total of 12 times for 30 days. The graph shows the quantification of the tumor masses of each group (day 30) (*p< 0.05, NM, n=6; IL-6, n=8). (C) Body weight changes after treatment with vehicle or IL-6. No significant difference in mouse body weight was observed during treatment. (D) Immunofluorescence staining for the TUNEL analysis of the implanted OCUM-2MD3 cells in each group. The graph shows the quantification of the positive staining rate (*p< 0.05, n=3). (E) WB analysis of p-STAT3 and Bcl-2 levels in the implanted OCUM-2MD3 cells in each group. The graph shows the normalization of p-STAT3 levels to total STAT3 levels and the normalization of Bcl-2 levels to total β-actin levels (*p< 0.05, n=3). (F) Body weight changes after treatment with S-CAF-CM or Ezh2 O/E-CAFs-CM. No significant difference in mouse body weight was observed during treatment.

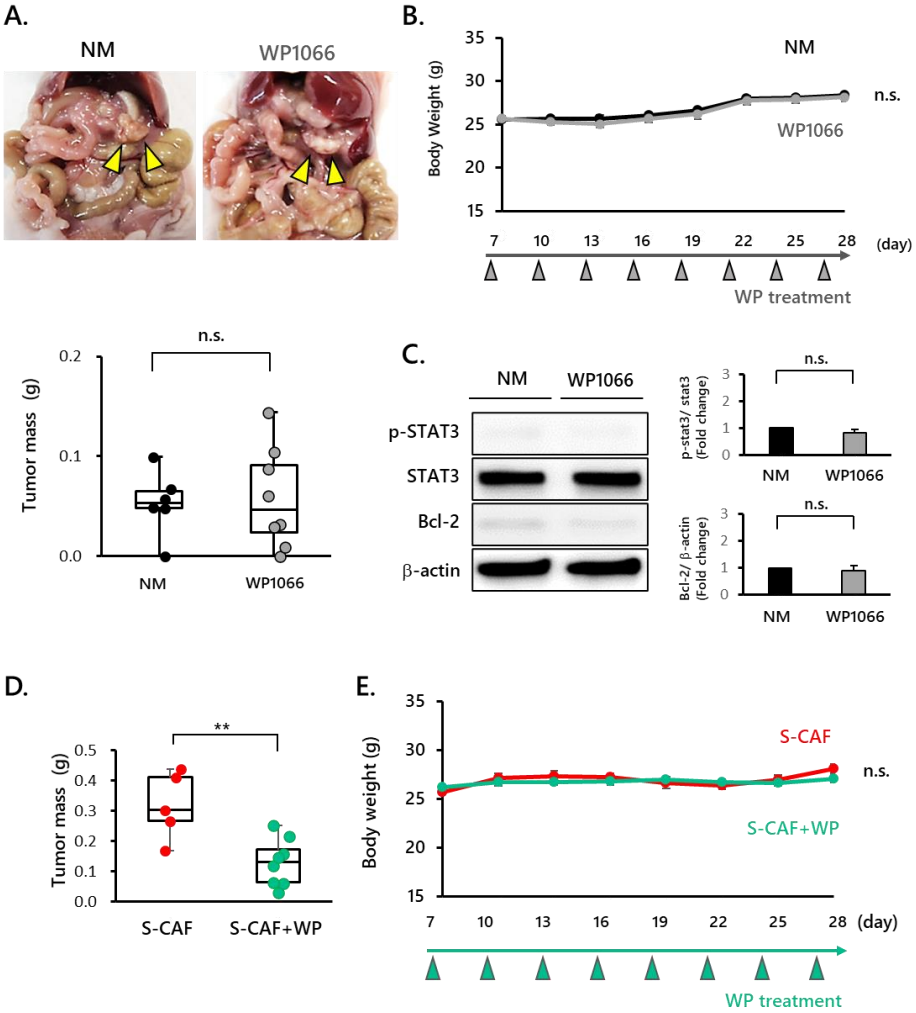

Supplementary Figure 7. The JAK/STAT3 inhibitor effectively blocks the peritoneal tumor formation enhanced by S-CAFs, but have no effect on that without S-CAFs. Related to Figure 6.
(A) Representative images of OCUM-2MD3-bearing mice treated with vehicle (DMSO) or 20 mg/kg WP1066 a total of 8 times for 3 weeks. The graph shows the quantification of the tumor masses in each group (n.s., not significant, NM; n=6, WP1066; n=8). (B) Body weight changes after treatment with vehicle (DMSO) or WP1066. No significant difference in mouse body weight was observed during treatment. (C) WB analysis of p-STAT3 and Bcl-2 levels in implanted OCUM-2MD3 cells from each group. The graph shows the normalization of p-STAT3 to total STAT3 levels and the normalization of Bcl-2 to total β-actin levels (n.s., not significant, n=3). (D) The graph shows the quantification of the tumor masses in each group (**p< 0.01, S-CAF; n=5, S-CAF+WP; n=8). (E) Body weight changes after daily injections of S-CAF-CM and treatment with vehicle (DMSO) or WP1066. No significant difference in mouse body weight was observed after the WP1066 treatment.

Table S1. Antibody sources and concentrations related to STAR Methods. Related to Figure 1 to 6.

	Target	Manufacturer	Catalog number	Western blotting (dilution)	Immunohistochemistry (dilution)	Immunofluorescence (dilution)	Flow cytometry (dilution)
Primary	β-Actin	Cell Signaling Technology	4967	1:1000			
	GAPDH	Cell Signaling Technology	5174	1:1000			
	p16 INK4A	Abcam	ab108349	1:5000			
	p15 INK4B	Santa Cruz	sc271791	1:1000			
	Lamin B1	Abcam	ab16048	1:1000			
	α-Tubulin	Abcam	ab7291	1:5000			
	Histone3	Abcam	ab1791	1:10000			
	NFκB1 p65	Cell Signaling Technology	8242	1:1000		1:400	
	STAT3	Cell Signaling Technology	4904	1:2000			
	p-STAT3	Cell Signaling Technology	9145	1:2000	1:400		
	p38	Cell Signaling Technology	8690	1:1000			
	p-p38	Cell Signaling Technology	9125	1:1000			
	AKT	Cell Signaling Technology	9272	1:1000			

	p-AKT	Cell Signaling Technology	9271	1:1000			
	ERK1/2	Cell Signaling Technology	9102	1:1000			
	p-ERK1/2	Cell Signaling Technology	4370	1:1000			
	EZH2	Cell Signaling Technology	5246	1:1000			
	H3K27me3	Millipore	07-449	1:1000			
	Bcl-2	Cell Signaling Technology	2872	1:1000			
	γH2AX	Millipore	05-636			1:1000	
	pSTQ	Cell Signaling Technology	2851			1:400	
	Ki67	Spring Bioscience Corp	M3062		1:200		
	CD90	BioLegend	328110				1:50
	CD140a (PDGFRα)	BioLegend	323507				1:200
	CD326 (EpCAM)	BioLegend	324236				1:100
	CD45	TOMBO	20-0459-T025				1:25
Secondary	Anti-rabbit IgG-HRP	Cell Signaling Technology	7074		1:5000		
	Goat anti-mouse IgG-HRP	Santa Cruz	sc2005		1:5000		

	Alexa Fluor 488 Goat anti-rabbit IgG	Molecular Probes	A11008			1:200	
	Alexa Fluor 594 Goat anti-mouse IgG	Molecular Probes	A11005			1:200	

Table S2. Primer/probe information. Related to Figure 2 and 4.

Official Symbol	Alias	Forward Primer	Reverse Primer	Universal Probe Library Probes (Roche Diagnostics) (dilution)
ACTB	β-actin	attggcaatgagcggtt	cgtggatgccacaggact	#11
IL6		caggagcccagctatgaact	gaaggcagcaggcaacac	#7
CCL20		gctgctttgatgtcagtgct	gcagtcaaagttgcttgctg	#39
CSF2		cagccactacaagcagcact	ccggtctcactcctggac	#3
IL8		agacagcagagcacacaagc	atggttccttccggtggt	#72
VEGFA		cctccgaaaccatgaacttt	atgattctgccctcctcctt	#22
EGF		gctggggatggaaaactatg	cttcggtgttgatgcacttg	#16
RHBDF2	iRhom2	gggcaaactcagactcgaag	tcccgccattcttgtcag	#51
IL7R		aaagttttaatgcacgatgtagctt	tgtgctggataaattcacatgc	#72
CADM1		ggtggttcaaagggaacaca	cacagtgtacatgtctgaccactc	#10
TM4SF1		tttctggcatcgtaggaggt	ccagcccaatgaagacaaat	#51
RELA	NFκB p65	cgggatggcttctatgagg	ctccaggtcccgcttctt	#47
STAT3		gagcagagatgtgggaatgg	cggtctcaaaggtgatcagg	#17

Table S3. Antibodies used for mass cytometry. Related to Figure 4.

Target	Metal tag	clone		Manufacturer	Catalog number	
CD90	159Tb	5E10		Fluidigm	3159007B	For cell surface molecules
PDGFRα (CD140A)	160Gd	D13C6		Fluidigm	3160007A	
CD326 (EpCAM)	141Pr	9C4		Fluidigm	3141006B	
CD45	89Y	HI30		Fluidigm	3089003B	
CD4	176Yb	RPA-T4		Fluidigm	3176010B	
CD8a	146Nd	RPA-T8		Fluidigm	3146001B	
CD11b (Mac-1)	167Er	ICRF44		Fluidigm	3167011B	
IL-6	147Sm	MQ2-13A5		Fluidigm	3147002B	For cytoplasmic molecules
CDKN2A/ p16INK4a	143Nd	EPR1473	Anti-CDKN2A/p16INK4a antibody [EPR1473] – BSA- and azide-free (ab186932)	Abcam	ab186932	For nuclear molecules